Available online at www.sciencedirect.com
ScienceDirect
Geochimica et Cosmochimica Acta 71 (2007) 2637–2655
Geochimica et Cosmochimica Acta
www.elsevier.com/locate/gca

New high-pressure and high-temperature metal/silicate partitioning of U and Pb: Implications for the cores of the Earth and Mars

Valérie Malavergne [a,b,*], Martine Tarrida [b], Rossana Combes [b], Hélène Bureau [c], John Jones [d], Craig Schwandt [e]

[a] *Lunar and Planetary Institute, 3600 Bay Area Boulevard, Houston, USA*
[b] *Laboratoire des Géomatériaux, Université de Marne La Vallée, 77454 Marne la Vallée, France*
[c] *LPS – CEA-CNRS, CE Saclay, 91191 Gif s/Yvette, France*
[d] *Johnson Space Center NASA, Houston, USA*
[e] *Jacobs Sverdrup/ESCG., P.O. Box 58447, Code JE23, Houston, USA*

Received 23 May 2006; accepted in revised form 19 March 2007; available online 24 March 2007

Abstract

In order to quantify possible fractionation of U and Pb into a metallic core, we have performed piston cylinder and multi-anvil press experiments at high pressure (up to 20 GPa) and high temperature (up to 2400 °C) and obtained the distribution coefficient $D_{\text{metal–silicate}}$ and the exchange partition coefficient $K_{\text{metal–silicate}}$ for these elements between metal and silicates (mineral or liquid). $D^{\text{Pb}}{}_{\text{metal–silicate}}$ and $D^{\text{U}}{}_{\text{metal–silicate}}$ depend strongly on the S content of the metallic phase, and also on the oxygen fugacity, in agreement with an effective valence state of 4 for U in silicates and 2 for Pb in silicates. $K^{\text{Pb}}{}_{\text{d metal–silicate}}$ and $K^{\text{U}}{}_{\text{d metal–silicate}}$ show no discernable pressure and temperature trend. U remains lithophile even at high pressure and high temperature but its lithophile nature decreases at very low oxygen fugacity. From our experimental data, it was possible to calculate the U and Pb contents of the cores of Mars and Earth under core-mantle equilibrium conditions at high pressure and high temperature. From the $D_{\text{metal–silicate}}$ of the present study, we obtained that: 0.008 ppm $< \text{Pb}_{\text{in the core}} <$4.4 ppm, and 0.0003 ppb $< \text{U}_{\text{in the core}} <$ 0.63 ppb, depending on whether the metal is S-free or S-saturated respectively, and if the mantle was molten or solid during the segregation process of the Earth's core around ΔIW-2. For Mars, based on a core segregation process around ΔIW-1, we obtained that: 0.005 ppm $< \text{Pb}_{\text{in the core}} <$ 3 ppm, and 0.00002 ppb $< \text{U}_{\text{in the core}} <$ 0.05 ppb, depending on the metallic composition: S-free or S-saturated respectively.

Our results suggest that the low concentration of Pb in the terrestrial mantle could not be explained by an early Pb sequestration in the Earth's core even if S is the dominant light element of the core. If we assume a magma ocean scenario, U might produced a maximum value of 1.5% of the total heat budget of the core with a segregation occurring below ΔIW-3. The values found in the present study for U in the Martian core suggest that the magnetic field activity of Mars before ~0.5 b.y. after its formation would be difficult to ascribe to the decay of U alone.

1. INTRODUCTION

Geologists and geochemists have been studying the abundance and distribution of the isotopes of uranium for more than a century. In order to understand how U is distributed in planets, the abundances and isotopic characteristics of lead (the radiogenic daughter of U^{235} and U^{238}) are useful parameters. Pb has a relatively low abundance in the primitive Earth's mantle in comparison with meteorites.

The first terrestrial Pb-isotope paradox refers to the fact that on average, rocks from the Earth's surface plot significantly to the right of the meteorite isochron in a common

* Corresponding author. Fax: +33 149 329 137.
E-mail address: malaverg@univ-mlv.fr (V. Malavergne).

0016-7037/$ - see front matter © 2007 Elsevier Ltd. All rights reserved.
doi:10.1016/j.gca.2007.03.011

Pb-isotope diagram (e.g. Allègre, 1982; Kramers and Tolstikhin, 1997). The Earth, however, should plot close to the meteorite isochron, implying the existence of at least one terrestrial reservoir that plots to the left of the meteorite isochron. That difference could be explained by Pb's volatile nature and tendency to combine with Fe–FeS due to its chalcophile behavior (e.g. Jones and Drake, 1986; Wood and Halliday, 2005). Thus, Pb could be lost during planetary accretion and core segregation (Allègre, 1982).

Compared to the Earth's mantle, Pb seems to be enriched in the Martian mantle by at least a factor of 2.5, as has been found for all other moderately volatile elements (Dreibus and Jagoutz, 2002). Thus, during the formation and evolution of Mars, Pb might have behaved more like a volatile and less like a chalcophile element. The difference of Pb's behavior between Earth and Mars should be studied carefully. In particular, the Martian core is supposed to be sulfur-rich (e.g. Wänke and Dreibus, 1994; Lodders and Fegley, 1997; Fei and Bertka, 2005), and Pb should, therefore, enter easily into the metallic core during the segregation process. The fact that the first estimation of Pb in the Martian mantle suggests that the chalcophile nature of Pb would not be dominant during the martian accretion implies that the chalcophile behavior of Pb as a function of pressure and temperature must be known. This is the first goal of this experimental study.

In parallel, many authors have discussed the possibility that U–Th radioactive decay might be an important heat source within planetary cores (e.g. Furst et al., 1982; Murrell and Burnett, 1982, 1986; Feber et al., 1984; Labrosse et al., 2001). Using the maximum acceptable difference in Th/U ratio between Earth's mantle and chondrites, one can obtain maximum values of 5 ppb U and 0.17 ppb Th in the core (Labrosse et al., 2001). Another radioactive element has long been considered an important heat source for the cores of terrestrial planets: the potassium. This latter element has been more experimentally studied over the last decade (e.g. Ito et al., 1993; Chabot and Drake, 1999; Gessmann and Wood, 2002; Lee and Jeanloz, 2003; Murthy et al., 2003; Hirao et al., 2006; Bouhifd et al., 2007) than U and Th. K was more extensively studied essentially because it has long been known that the Earth's mantle is more depleted in potassium, than C1-chondrites (e.g. Wasserburg et al., 1964). Like for Pb, the K depletion in the Earth's mantle could be explained by two major mechanisms: the potassium volatility during the early stages of accretion, or an incorporation into the core during the metal segregation. According to estimates of the heat source necessary in the Earth's core to maintain the observed magnetic field (Gubbins et al., 1979), around 1000 ppm of K in the core could supply enough energy by itself without any other radioactive heat sources such as U and Th. Unfortunately, the previous studies, which determined the partition coefficients of K between metal and silicate, are not in a good global agreement, with some studies showing that K could significantly enter the core (e.g. Hirao et al., 2006; Bouhifd et al., 2007) while others showed the opposite behavior (e.g. Chabot and Drake, 1999). These contradictory results reflect the fact that the partition coefficients of elements are known to be dependent on pressure, temperature, oxygen fugacity, and silicate and metallic compositions. These thermodynamic variables can have a large effect on the partition coefficient evolution. Then, the presence of K in the core is possible, but not yet a certainty. The heat sources for terrestrial planetary cores are thus not fully understood, we still need constraints from others radioactive elements, such as Th and U. Previous studies (Murrell and Burnett, 1982, 1986) have shown that, under reducing conditions, U and Th deviated from lithophile character and concentrated in sulfides. First, enstatite chondrites have strong concentrations of U and Th into oldhamite (CaS) (Furst et al., 1982; Murrell and Burnett, 1982) showing that under the reducing conditions that prevailed during the enstatite chondrites formation, U and Th could be concentrated in sulfides. Secondly, piston cylinder partitioning experiments on U and Th between liquid Fe–FeS and basaltic or granitic liquid silicate compositions suggest that U could prefer sulfide to silicate at very low fO_2 (Murrell and Burnett, 1986). These authors suggested that U and Th should also be considered in discussions of radioactive heating of planetary cores despite their strong lithophile character at high fO_2. If a first accretion stage took place under highly reduced conditions (Wänke et al., 1984; Javoy, 1995), then, it is important to understand the behavior of radioactive elements under such conditions. U and Th could be incorporated into the metal of the core only if they are siderophile enough under the (P, T, fO_2) conditions of this early segregation stage. Wheeler et al. (2006) have made piston-cylinder and multi-anvil experiments where D_U between metal and silicate melts has been determined between 1–10 GPa and 1750–2300 °C under reducing conditions. Their results indicate that: (1) U remains lithophile at fO_2 2log unit below the Iron-Wustite (IW) buffer even with up to 28 wt% of S in the metallic liquid, (2) their maximum value is 0.01, with such values U would have no importance to the Earth's core budget. New experimental studies are still needed for U in order to understand its evolution with redox conditions, which could be a fundamental parameter during planetary accretion (e.g. Wänke et al., 1984; Javoy, 1995; Chabot et al., 2005; Wade and Wood, 2005). The second goal of the present study is thus to determine more precisely the partition coefficient of U between metal and silicates at higher pressure and temperature and under a wide range of redox conditions.

Several lines of evidence suggest that the cores of the Earth and the Mars possess a significant proportion of light elements (e.g. Poirier, 1994; Allègre et al., 1995, 2001; Buffett, 2000; Gudkova and Zharkov, 2004). The light components could be constrained from determining the physical conditions of core formation in these early planets. The Earth and Mars could have been formed through accretion of many small differentiated bodies (e.g. Kokubo and Ida, 2000). In this model, the cores of these differentiated objects might have sunk to the center of the planet experiencing little interaction with the (solid or liquid) silicates of the mantle. An alternative model envisages a homogeneous accretion (Li and Agee, 1996; Righter and Drake, 1997, 2000; Gessmann and Rubie, 2000; Li and Agee, 2001; Chabot and Agee, 2003; Righter, 2003; Chabot et al., 2005)

where the metal of the core would have been in equilibrium with a molten mantle at the base of a magma ocean before it sank directly to the Earth's center. Other models explores the idea that metal–silicate equilibrium is attained by equilibration between metal droplets and silicate melt (Stevenson, 1990; Karato and Murthy, 1997; Rubie et al., 2002). A third model incorporates aspects of different scenarios where a giant impact might have melted the mantle after a first phase of equilibrium between metal and silicate, then Pb entered the Earth's core at the latest stage of core formation (Wood and Halliday, 2005). Regardless of the model, it appears that interaction between metal and silicates at moderate pressures (i.e. 0–30 GPa) may have played an important role in the planetary formation. The incorporation of light elements might have taken place under these conditions at high temperature and variable oxygen fugacity (e.g. Wänke et al., 1984; Javoy, 1995; Wade and Wood, 2005). Experimental simulations which are able to reproduce this range of pressure and temperature under variable redox conditions are necessary.

The partition coefficients of Pb and U between liquid metal and silicates have been investigated at different oxygen fugacities, with different starting silicate and metal compositions at pressures between 5 and 20 GPa and temperatures between 1665 and 2400 °C. In order to be relevant to the light elements of the Martian or Earth's cores, we have performed experiments with (Fe, S), (Fe, Si) but also with (Fe, S, Si) metallic phases, as S is a possible candidate for these planetary cores (e.g. Poirier, 1994; Gudkova and Zharkov, 2004; Fei and Bertka, 2005), and Si is a good candidate for the light element in the Earth's core (e.g. Wänke et al., 1984; Poirier, 1994; Allègre et al., 1995, 2001; Javoy, 1995; Malavergne et al., 2004).

2. EXPERIMENTAL AND ANALYTICAL PROCEDURES

The starting silicates were a natural San Carlos pyroxene and a silicate glass which has the composition of a simplified CI chondrite (Bouhifd and Jephcoat, 2003). The compositions of these starting silicates are reported in Table 1. The other starting materials, used in the present study, are: Si, Fe, FeS, UO_2 and PbO, all from Goodfellow™ with purities of over 99.99%. These components were mixed in different proportions in order to investigate various redox conditions and various dilution conditions for U and Pb. The contents of UO_2 and PbO added in the samples varied between 0.9 and 0.02 wt%, but were always below 1 wt% in order to stay as close as possible in the validity field of Henry's law.

Table 1
Compositions of the synthetic glass and the San Carlos pyroxene used as starting silicates in the present study (EPMA analysis)

Wt%	Glass	SC Enstatite
Si	24.00	25.67
Al	0.99	2.75
Fe	4.88	5.96
Mg	22.10	18.77
Ca	2.16	0.66
O	45.87	46.19

All the 20 GPa multianvil experiments were performed at the Bayerisches Geoinstitut, Bayreuth, Germany using a 1200-ton press. The other multi-anvil experiments were carried out in the press of the Laboratoire Magmas et Volcans in Clermont-Ferrand (France), using a 1000-ton press at 1900 °C and a pressure range from 5 to 15 GPa. 14/8 and 10/5 assemblies (octahedra side-length/WC cube truncation edge-length) were used. High pressure assemblies consisted of Cr-doped MgO octahedra containing a cylindric $LaCrO_3$ heater and pyrophyllite gaskets. Temperature was monitored with a $W_3Re/W_{25}Re$ thermocouple located axially with respect to the heater and with the junction in direct contact with the MgO or graphite capsule. Pressure calibrations for these experimental configurations are given in Hammouda (2003) and Tronnes and Frost (2002). The *P–T* uncertainties are estimated to be ±0.5 GPa and ±100 °C, except for #2309(±200 °C) where the temperature, 2400 °C, was estimated by extrapolating the relation between temperature and power supply constructed to 2200 °C and from previous runs, as already done in previous multi-anvils studies (e.g. Ito et al., 2004; Nishihara et al., 2005). Additional errors due to the lack of knowledge of pressure effects on the emf of the thermocouple are generally believed to be less than ±30 °C (Li et al., 2003). The sample powders were contained in either MgO single crystal or graphite capsules surrounded by polycrystalline MgO, which was fired at 1000 °C before the experiment. The H_2O content of the sample was minimized by preliminary heating of the entire assembly for about 12 h at 220 °C in an oven. Pressure was first raised to the desired value, then temperature was increased at a rate of 100 °C/min. Typical run durations were a few minutes. Details of the experiments are listed in Table 2. The charges were quenched by switching off the electrical power resulting in a temperature drop to below 500 °C in less than 3 s. The samples were then decompressed overnight (12 h), then mounted in epoxy, sectioned, and polished for analysis.

The piston cylinder experiments were carried out using the Lunar and Planetary Institute QuickPress at the NASA Johnson Space Center (Houston, Texas, USA). These experiments were completed in a non-end loaded, 12.7 mm piston cylinder apparatus with single-sleeve $BaCO_3$cell assemblies (e.g. McDade et al., 2002) and graphite furnace and capsule. Temperatures were measured with a $W_{95}Re_5 - W_{74}Re_{26}$ thermocouple, separated from the capsule by an alumina disc. No pressure correction was made for the thermocouple emf. The pressure calibration details of this press are given in Musselwhite et al. (2006).

Samples were first studied with a LEO STEREOSCAN 440 Scanning Electron Microscope (SEM) with PRINCETON GAMMA-TECH (PGT) SPIRIT energy-dispersive X-ray analyzer (EDX), and Raman spectroscopy. The Raman measurements were carried out on a T64000 Jobin-Yvon confocal microRaman spectrometer equipped with the CCD detector. The 514.532 nm of a coherent 70 Ar^+ laser was used for sample excitation. This line operated at 0.2 W. The integration time was between 60 and 120 s. All the spectra were recorded between 200 and 1400 cm^{-1}.

Table 2
Experimental conditions and phases observed

Sample	*P* (GPa)		*T* (°C)	Duration (mn)	Capsule	Metal	Silicate	Proportion of metal in the starting material (wt%)	Major observed phases	ΔIW
#3562	20	MA	2200	5.5	C	Fe–S–Si	Glass	30	Met–maj	−6.4
#3563	20	MA	2200	3.2	C	Fe–S	Glass	10	Met–maj	−2.1
#3566	20	MA	2200	5	C	Fe–Si	Px	25	Met- maj	−3.8
#3565	20	MA	2200	5	C	Fe–S	Px	20	Met–maj	−2.4
#2309	15	MA	2400	5.5	C	Fe–Si-S	Px	21	Met–SL	−4.8
#282	15	MA	1900	8	C	Fe–Si	Glass	30	Met–maj	−3.2
#412	15	MA	1900	9	C	Fe–Si–S	Px	20	Met–maj	−3.7
#279	15	MA	1900	10	C	Fe–S	Px	11	Met–maj	−2.9
#414	5	MA	1900	6	MgO	Fe–Si	Glass	30	Met–SL	−5.4
#92	1.5	PC	1700	25	C	Fe–Si	Glass	30	Met–Px	−6.2
#90	1.5	PC	1700	25	C	Fe–Si	Px	36	Met–SL	−4.7
#96	1.5	PC	1665	25	C	Fe–S	Glass	20	Met–SL	−2.3

Met, metal; SL, silicate liquid; Px, pyroxene; maj, majorite; PC, piston-cylinder experiments; MA, multianvil experiments. ΔIW, log(fO_2) relative to IW buffer (see text for more details).

CAMECA SX-50 and SX-100 electron probe microanalyzers (EPMA), equipped with wavelength dispersive X-ray spectrometer (WDX) were used to analyze the samples. Four monochromators detected the first order reflection of Kα, Mα or Mβ emission lines: TAP for Mg, Al, Si, PET for Ca, S, Pb and U, sometimes LIF for Pb and LLIF for Fe. The counting times for the major elements were 10 s or 20 s and a typical beam current of 10 nA was used at 15 kV. Multiple analyses with a 10–20 μm defocused beam were used to determine the bulk compositions of the silicate melt and liquid metal because of the quench textures present in these phases (see Section 3 for more details about the quench structures). Thus, the silicates of the samples #2309, #414, #90 and # 96 (Table 2) were analyzed with this defocused procedure and the metallic phases of each sample as well. The mean compositions of these phases, which are re-

Table 3
Averages of the metallic phases compositions (in wt%) determined by EPMA and μPIXE

Sample		Fe	Si	S	Pb	U (ppm)	Total	*N*[a]
#3562	*EPMA*	63.6 ± 0.6	8.6 ± 0.2	23.3 ± 0.3	1.10 ± 0.03	2.1 wt% ± 0.05	96.81	60
#3563	*EPMA*	54.0 ± 0.5	0.16 ± 0.02	38.1 ± 0.5	6.9 ± 0.9	170 ± 40	99.18	30
#3566	*EPMA*	91.5 ± 0.2	5.5 ± 0.1	—	0.33 ± 0.04	1000 ± 170	97.33[d]	38
#3565	*EPMA*	60.6 ± 0.8	0.18 ± 0.03	35.5 ± 0.4	1.43 ± 0.09	—	97.71	25
#2309	*EPMA*	67.7 ± 1.1	26.6 ± 0.7	2.33 ± 0.7	0.09 ± 0.02	46 ± 18	97.33[e]	60
#2309	*EPMA*	54.6 ± 1.5	1.53 ± 0.07	33.3 ± 0.8	7.1 ± 0.9	250 ± 42	100.3[f]	60
#282	*EPMA*	92.0 ± 0.8	5.14 ± 0.07	—	0.22 ± 0.03	50 ± 13	97.36	35
#282	μ-*PIXE*	—	—	—	0.299 ± 0.07	<70 (DL)	—	[b]
#412	*EPMA*	51.25 ± 1.01	0.92 ± 0.02	39.20 ± 0.08	6.45 ± 0.9	—	97.82	30
#412	*EPMA*	79.0 ± 1.2	17.05 ± 0.35	1.23 ± 0.04	0.083 ± 0.022	—	97.36	30
#279	*EPMA*	53.0 ± 0.8	0.1 ± 0.01	41.1 ± 0.6	4.1 ± 0.6	45 ± 21	98.3	60
#279	μ-*PIXE*	—	—	—	3.83 ± 0.8	<160[c]	—	[b]
#414	*EPMA*	89.1 ± 0.5	9.05 ± 0.1	—	0.28 ± 0.05	86 ± 17	98.44	70
#92	*EPMA*	86.1 ± 0.4	10.4 ± 0.1	—	0.039 ± 0.06	—	96.54	60
#90	*EPMA*	90.0 ± 0.4	6.8 ± 0.1	—	0.12 ± 0.02	—	96.92	75
#96	*EPMA*	58.5 ± 0.4	0.5 ± 0.1	35.1 ± 0.5	2.3 ± 0.4	—	96.4	90
2σ								

All the EPMA reported concentrations are the mean values of *N* analysis.
No significant oxygen was detected in the metal. However, the presence of small amount of oxygen (<0.1 wt%) in the metal can not be ruled out. The presence of C is likely (except in #414 where a MgO capsule was used) but not measurable with EPMA.
Errors are ±2 standard deviations of the mean.

[a] Number of analysis, DL means detection limit: the actual concentration is below.

[b] For the μ-PIXE analysis the concentrations are calculated (according to Maxwell et al., 1989) from selected areas extracted from the maps using (Daudin et al., 2003) and corresponding to the different metallic phases present in the samples.

[c] The actual value of U could not be determine precisely because of the small sizes of a lot of metallic phases allowing a systematic contamination by the silicate.

[d] Some Cr (1 wt%), Mn (0.27 wt%), Co (0.1 wt%) and Ni (0.4 wt%) were also detected in the metal increasing the total number.

[e] Some Cr (0.16 wt%), Mn (0.09 wt%) and Ni (0.36 wt%) were also detected in the metal increasing the total number.

[f] Some Cr (3.6 wt%), Mn (1.2 wt%) and Ni (0.09 wt%) were also detected in the metal increasing the total number.

Table 4
Silicate phases compositions (in wt%) determined by EPMA and μPIXE

Sample		Fe	Si	Mg	Al	Ca	S	O	Pb (ppm)	U (ppm)	Total	N^a
#3562	*EPMA*	0.048 ± 0.01	27.0 ± 0.3	21.1 ± 0.2	3.1 ± 0.1	1.05 ± 0.03	0.05 ± 0.005	48.5	490 ± 53	240 ± 43	100.92	50
#3563	*EPMA*	4.70 ± 0.1	23.8 ± 0.2	21.0 ± 0. 2	2.2 ± 0.1	2.2 ± 0.1	0.12 ± 0.01	44.8	1800 ± 268	1430 ± 213	99.14	25
#3566	*EPMA*	0.82 ± 0.02	27.6 ± 0.3	19.9 ± 0.2	2.4 ± 0.1	0.60 ± 0.01	—	48.0	2700 ± 274	3000 ± 450	100.06[c]	30
#3565	*EPMA*	4.7 ± 0.07	25.6 ± 0.3	19.1 ± 0. 2	2.5 ± 0.1	0.6 ± 0.01	0.07 ± 0.004	45.7	540 ± 60	—	98.33	30
#2309	*EPMA*	0.3 ± 0.02	28.3 ± 0.9	18.9 ± 0.7	1.8 ± 0.06	0.9 ± 0.03	1.5 ± 0.05	48.5	750 ± 152	5320 ± 788	100.27[d]	60
#282	*EPMA*	1.38 ± 0.02	27.1 ± 0.3	21.5 ± 0.2	1.1 ± 0.1	1.2 ± 0.1	—	47.0	3500 ± 320	760 ± 119	99.71	50
#282	μ-PIXE	—	—	—	—	—	—	—	3470 ± 316	690 ± 140	—	[b]
#412	*EPMA*	0.73 ± 0.02	21.7 ± 0.2	21.8 ± 0.2	8.15 ± 0.1	0.25 ± 0.04	0.05 ± 0.02	46.9	650 ± 69	—	99.60	70
#279	*EPMA*	1.45 ± 0.02	27.25 ± 0.3	21.3 ± 0.2	1.20 ± 0.1	1.3 ± 0.1	0.06 ± 0.02	47.2	790 ± 83	447 ± 72	99.88	25
#279	μ-PIXE	—	—	—	—	—	—	—	690 ± 72	440 ± 92	—	[b]
#414	*EPMA*	0.22 ± 0.03	16.5 ± 0.6	37.1 ± 0.8	0.6 ± 0.1	0.8 ± 0.1	—	44.3	1490 ± 155	2008 ± 262	99.87	40
#92	*EPMA*	0.071 ± 0.008	26.7 ± 0.7	21.35 ± 0.7	2.15 ± 0.07	2.17 ± 0.08	—	47.4	70 ± 15	—	99.84	60
#90	*EPMA*	0.36 ± 0.02	24.1 ± 0.2	26.4 ± 0.3	1.6 ± 0.1	0.37 ± 0.02	—	46.7	700 ± 138	—	99.64	30
#96	*EPMA*	5.9 ± 0.3	22.2 ± 0.7	22.45 ± 0.7	2.45 ± 0.09	1.73 ± 0.1	0.3 ± 0.02	44.3	1600 ± 245	—	99.5	80

All the EPMA reported concentrations are the mean values of *N* analysis.
Errors are ±2 standard deviations of the mean.
[a] Number of analysis.
[b] For the μ-PIXE analysis the concentrations are calculated (according to Maxwell et al., 1989) from selected areas extracted from the maps corresponding to the different silicate phases present in the samples, according to Daudin et al. (2003).
[c] Some Cr and Mn have been also detected and represent 0.17 wt% of the total.
[d] Some Cr and Mn have been also detected and represent 0.07 wt% of the total.

ported in Tables 3 and 4, are the average of multiple analyses performed with a defocused beam. The major elements were analyzed first with these conditions. The analyzed total for metal obtained by EPMA ranges from 96.4 to 100.3 wt%, which shows a maximum weight deficit of 3.6 wt%. This could be partly due to the polished surfaces of the samples which were not always perfectly flat (polishing the multi-anvil samples enclosed in hard diamond capsules was challenging), but is more likely caused by the dissolution of C from the capsule material as mentioned by Chabot et al. (2005, 2006). The possible effect of C in our samples is discussed in Section 3. The O concentrations in the silicate were calculated based on standard valences for the measured major elements: 4+ for Si, 3+ for Al, 2+ for Fe, Mg, Ca. Errors were calculated as twice the standard deviation of the mean.

The trace elements were analyzed with EPMA under two different conditions, except for U, which could be properly analyzed at the highest voltage conditions only. The first condition of acquisition was: a counting time of 1000 s (which have been divided to 10 times 100 s in order to prevent radiation damage), a beam current of 500 nA at 30 kV with a spot size of 10 or 20 μm. Only trace elements were analyzed under these conditions, from the Mα or Mβ emission lines for Pb and U, respectively. Under such extreme conditions, the following detection limits can be obtained: 40 ppm for U and 60 ppm for Pb. The procedure for the calculation of concentrations is explained by Fialin et al. (1999) and was done exactly with the same method. The standards used were Fe_2O_3 for Fe, clinopyroxene for Si, Ca and Mg, orthoclase for Al, UO_2 for U, PbS for Pb. Samples containing no U were used as blanks (#90, #92, #96, #412 or #3565) for the U analyses. The concentrations of U in these samples were always well below the detection limit. The second condition of EPMA acquisition was: a counting time of 900 s, 50nA and 20 kV with a spot size of 5 or 10 μm. Under these conditions, it was impossible to properly analyze U, but a detection limit of 600 ppm for Pb could be reached. Thus, these last measurements allowed us to check the validity of our first Pb measurements made at 30 kV and 500 nA, event if the Pb concentrations of three samples (#3562, #3565, #92) were below the detection limit with these accelerating voltage and current. These two independent EPMA (the first one made in Paris, and the last one in Houston, but both using a CAMECA SX-100 or SX-50) gave the same average concentrations for Pb and the other elements but U, which was not analyzed in these last sessions.

For the samples #282 and #279, the concentrations of U and Pb in metal and in silicates have also been measured by μPIXE mapping (Particle Induced X-ray Emission) in the Laboratoire Pierre Süe, CEA Saclay (France) (Khodja et al., 2001). A 2 MeV proton beam of 400 pA intensity with a focused beam was scanned over the samples with a spatial resolution of 4 × 4 μm (scanning rate ranging from 500 to 1000 Hz). Fluorescence was detected with a Ge X-ray detector. The results were processed using the RISMIN software elaborated by Daudin et al. (2003), in order to extract selected areas corresponding to the different phases (metal or silicate). The chemical composition of each phase observed in the maps was calculated after the GUPIX software (Maxwell et al., 1989). Deposited charge ranged from 0.5 to 8 μC, depending on the analysis and the size of the map (250 × 270 to 8 × 10 μm^2). Typically, several hours of acquisition were needed to obtain a map. The concentrations of U and Pb in the silicates phases obtained by μPIXE mapping are in good

agreement with those obtained by EPMA, giving us more confidence in our first set of EPMA results.

3. RESULTS

3.1. Attainment of equilibrium in the samples

In each sample several chemical profiles have been made with EPMA in order to test local equilibrium. For all experiments, the largest particles of metal in contact with silicates have the same global composition as the smaller metal grains embedded within the silicate matrix. This is a first indication for local equilibrium at the scale of several tens of micrometers. A second indication is the homogeneity of the U contents in the metallic and silicate phases even though this element was initially present only as UO_2. A third indication is the absence of chemical zoning in the silicates. For the 4 samples where the silicate was melted at HP-HT, we recovered samples with silicate quenched structures (Fig. 1). The mean compositions of these silicates were constant in each sample. Nishihara et al. (2005) did multi-anvil experiments with mineral assemblages of silicates, which were well equilibrated, at up to 19 GPa and 1900 °C with maximum run durations of 10 min, conditions that are close to ours. Moreover, Ohtani et al. (1997), Gessmann and Rubie (1998), Malavergne et al. (2004) and Wheeler et al. (2006) have demonstrated attainment of equilibrium in similar experiments in less than 3 min. All our experiments have run durations longer than 5.5 min when the silicate phases stay in the solid state or more than 3 min when the silicate is liquid. Walker and Agee (1989) proposed that diffusion coefficients for major elements in liquid silicate are in the range of 10 to 1000 $\mu m^2/s$ at temperature between 1800 and 2800 K, and pressures between 15 and 25 GPa, which was well confirmed for Pb by the experimental work of Perez and Dunn (1996) who found the diffusivity (D_{Pb}) of Pb in a natural rhyolite at 1 GPa between 1000 and 1450 °C. If we extrapolate their D_{Pb}'s to higher temperature (up to 2000 °C), we found a value of 82 $\mu m^2/s$. For clinopyroxenes, the D_{Pb}'s have been determined by Cherniak (1998) over the temperature range 800–1100 °C. If we extrapolate again the D_{Pb}'s of Cherniak (1998) to higher temperature (up to 2000 °C), we found that diffusion coefficients of Pb are in the range of 10 to 180 $\mu m^2/s$, depending on the iron content of the pyroxene. If these coefficients are used at higher pressure, we find that Pb should have been well diffused in the silicates of our experiments even after just 5 min. Another argument in favor of the equilibrium is based on the study of Zheng et al. (2003) and Monchoux and Rabkin (2002) where values of diffusivity in metallic melts are given. Typical values for diffusivity in many metallic melts are in the range of 10^{-8}–10^{-9} $m^2\ s^{-1}$ showing that the solute elements (here U and/or Pb) present in the liquid metal diffuses rapidly in the metallic phase. After 3 min, all the solute elements present in metallic melts are well homogenized. Thus, the limiting diffusivity value here is the diffusion in solid mineral. The uranium diffusion coefficient for diopside ranges from 0.0001 $\mu m^2/s$ at 1240 °C (Seitz, 1973) to 0.0007 $\mu m^2/s$ at 2000 °C (Van Orman et al., 1998) and unfortunately the U diffusion values are not known for the minerals of the present study. But, it seems obvious that U could have difficulties equilibrating in our experiments if the diffusion coefficients of U in pyroxene and majorite are as low as in diopside. However, the U contents in the silicates of the present study are always homogeneous, like in the recent study of Wheeler et al. (2006). Meanwhile in Wheeler et al. (2006) experiments are on two liquids, which is the case for only for four samples in the present study. Finally, it is important to understand that equilibrium in our samples is not based totally on the diffusion processes of U and Pb, but also on the kinetics of oxidation and reduction reactions. We can not exclude the possibility that maybe we have underestimated the diffusion rates of U in minerals at HT, as they are not known for the majorite and pyroxene under the P–T conditions of our experiments. The chemical homogeneity of U in the minerals and in the metallic phases remains the best argument to demonstrate that chemical equilibrium was reached in the samples of this study.

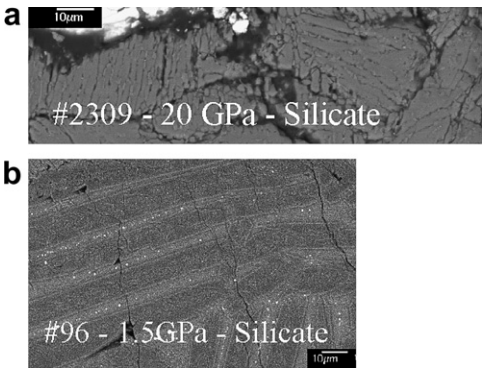

Fig. 1. backscattered electron image of two typical quenched silicate structures: (a) from sample #2309 (20 GPa–2400 °C), (b) from the sample #96 (1.5 GPa–1665 °C). The quenched structures are finer in the highest pressure run.

3.2. General features of the samples

Under the pressure–temperature conditions of our experiments (Table 2), the metal was always liquid, as found in previous studies: the melting data of Siebert et al. (2004) and Sanloup and Fei (2004) for the Fe–S–Si system, the data of Kuwayama and Hirose (2004) and Malavergne et al. (2004) for the Fe–Si system, the data of Usselman (1975) and Fei et al. (1997, 2000) for the Fe–S system. The compositions of the metallic phases and silicate phases are reported in Tables 3 and 4. Typical views of the entire samples are shown in Fig. 2.

The silicates were usually solid, particularly in the experiments where San Carlos pyroxene was used as the starting silicate composition (with the exception of #2309 at 2400 °C). Silicate liquid was observed in four experiments. We know silicate melt was present in the 1.5, 5 GPa and one 20 GPa experiments (#90, #96, #414 and #2309) because characteristic dendritic microstructures were observed (Fig. 1). In all the samples of this study, the Fe content Fe# (Fe# = Fe/(Fe + Mg) molar ratio) of the silicates decreased strongly by 80–95% showing that the

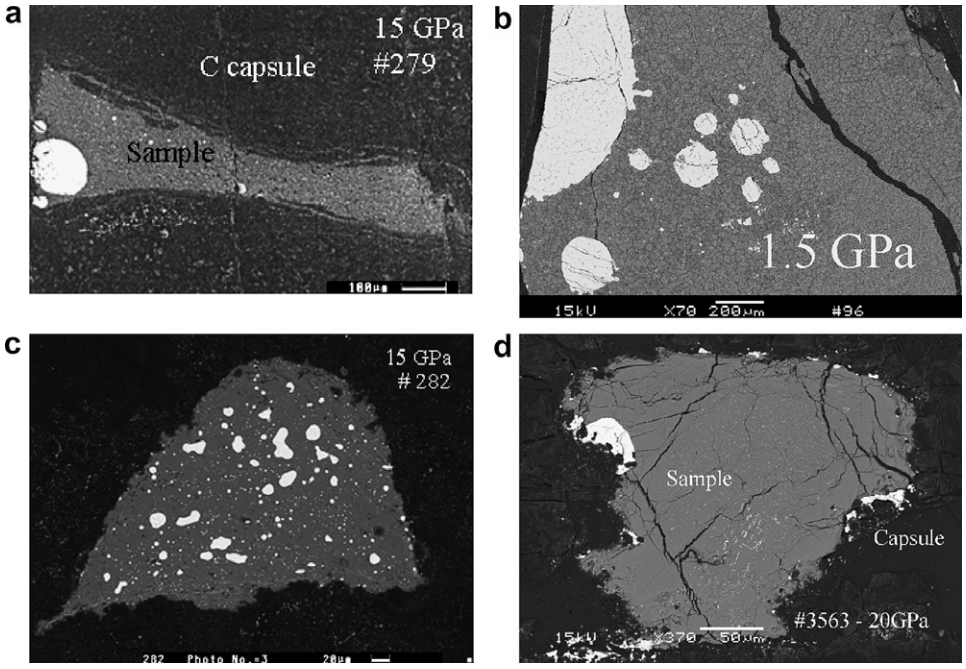

Fig. 2. backscattered electron image of four typical entire samples: (a) #279: 10 GPa–1900 °C, the scale bar represents 100 μm, (b) #96 (1.5 GPa–1665 °C) the scale bar represents 200 μm. (c) #282: 10 GPa–1900 °C, the scale bar represents 20 μm, (d) #3563: 20 GPa–2200 °C, the scale bar represents 50 μm.

silicate starting material has been reduced, except for sample #96 which was the least reduced run. The silicate in the 20 and 15 GPa runs is majorite, as revealed by their compositions (Table 4) and Raman spectra (Fig. 3). This observation is in good agreement with the phase diagram of $MgSiO_3$, the phase diagram in the system SiO_2–MgO–Al_2O_3–CaO (Gasparik, 2003, pp. 24 and 164), and in the system Na_2O–CaO–FeO–MgO–Al_2O_3–SiO_2 determined between 13 and 15 GPa (Gasparik, 2000) where the transformation from clinopyroxene to silica-rich garnet has been characterized as almost isochemical and close to $Na_{0.8}Ca_{0.3}(Mg, Fe)_{2.25}Al_{0.5}Si_{4.15}O_{12}$.

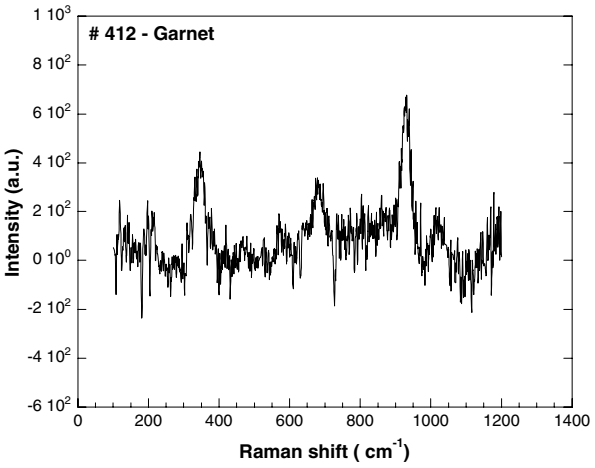

Fig. 3. Raman spectrum of silicate in sample #412. This spectrum is in good agreement with the spectrum of majorite garnet obtained by Gillet et al. (1992).

Another particular point is the MgO enrichment in the sample #414 compared to other samples which were made using the same starting silicate, but not the same capsule. The run #414 was contained in a MgO capsule while the others were contained in graphite capsules. The silicates of #412 are also enriched in Al compared to the starting composition. The increase in the Al content of these silicates is likely the result of a reaction between the ceramic of the thermocouple of the cell assembly and the silicate of #412, as was observed in a previous similar study (Malavergne et al., 2004). The metallic phase was most often of quasi-spherical shape within the silicate matrix. The metallic phases were rarely homogeneous because of liquid immiscibility or quench effects. Four typical microstructures have been characterized.

3.2.1. Immiscibility and quench effects with the major elements (Fe, S, Si) (samples #412, #2309 and #3562)

In the samples #412, #3562 and #2309, a mixture of FeS and Si were used as the starting metallic composition, so these two phases were well separated prior to the run. These two phases FeS and Si have coalesced into single metallic blobs (Fig. 4) after reaction at high pressure (HP) and high temperature (HT). Two kinds of microstructures have been characterized. First, in the samples #412 and #2309, SEM images reveal that the metal of these runs contains two separated phases: a Fe–S rich, Si-poor phase and a Fe–Si rich, S poor phase (Fig. 4). In Fig. 4a, the texture of the two different metallic liquids can be seen: the Fe–Si rich, S poor phase is always separated to the Fe–S rich, Si-poor phase. This picture clearly shows two liquids, a behavior known in natural systems like in chondrites where FeS and Fe-rich

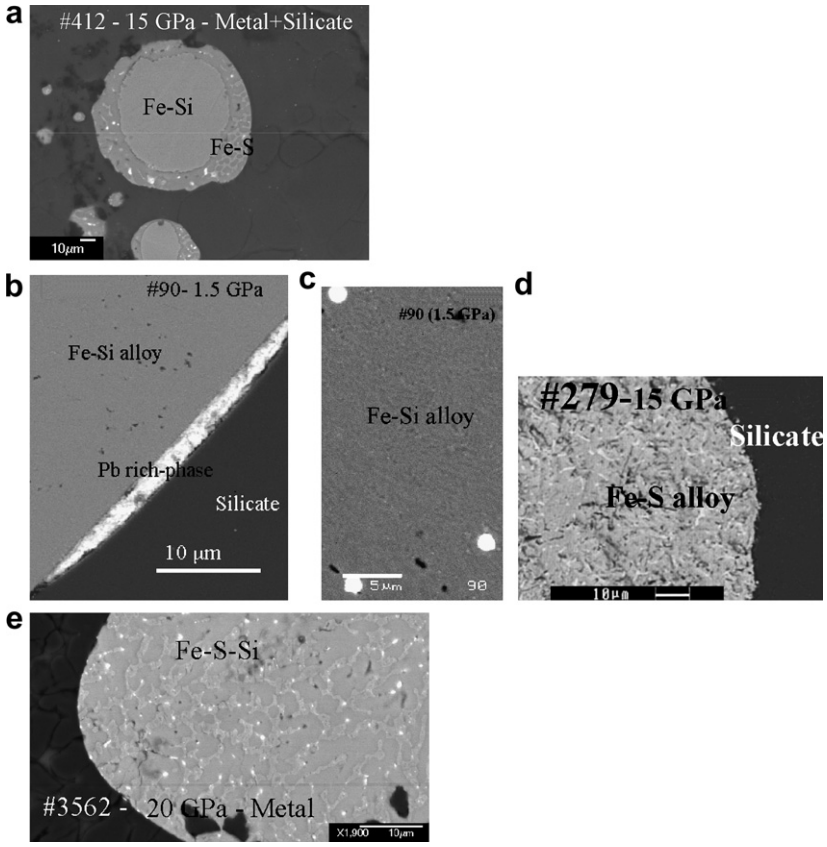

Fig. 4. Backscattered electron image of (a) a typical metallic phase in the samples #412 (15 GPa–1900 °C). This metal contains two immiscible metallic liquids: a Fe–S rich, Si-poor phase and a Fe–Si rich, S poor phase. A Fe–S rich, Si-poor metallic crown is formed around the Fe–Si rich, S poor metallic phase. The Fe–S-rich liquid shows similar textures than the one of (d) in the binary Fe–S. The Fe–Si-rich liquid shows similar textures than the one of (b) in the binary Fe–Si. (b) sample #90 (1.5 GPa–1700 °C) where a Pb-rich vein is observed as tiny vein around the Fe–Si metallic matrix. The Fe–S metallic phases and Pb-rich alloy were always together in the whole sample. (c) #90, enlargement of the Fe–Si alloy (seen in (b)) where tiny spherical particles of Pb-rich phase can be found as micro-scale spherical particles embedded in the alloy matrix. (d) #279 (15 GPa–1900 °C) Pb-rich tiny bright veins are observed in the Fe–S metallic matrix. These typical textures were formed during the quench of a single metallic liquid. (e) #3562 (20 GPa–2200 °C) a Fe–S–Si metallic phase is observed with typical quenched structures.

metal are present as two separate phases. The textures in the metallic phases of #412 and #2309 are thus consistent with two immiscible liquids, a feature well characterized at atmospheric pressure in metallurgical system (Raghavan, 1988).

Secondly, the textures of the run #3562 are different from those characterized above, since the two metallic phases were mixed and more like an emulsion of two liquids (Fig. 4e) as observed by Siebert et al. (2004) with similar metallic compositions, pressure and temperature. Moreover, the similarities in the metallic textures of previous studies where quench structure were characterized (e.g. Sanloup and Fei, 2004, 2005; Sanloup and Fei, 2004; Kuwayama and Hirose, 2004; Siebert et al., 2004; Tsuno et al., 2007) with the Fig. 4d and e strengthen the conclusion that in samples #3562 and #279 there were quenched structures. The Fe–S-rich liquid of the Fig. 4a shows similar textures than the one of the Fig. 4d in the binary Fe–S. The Fe–Si-rich liquid of the Fig. 4a shows similar textures than the one of the Fig. 4b in the binary Fe–Si. This observation confirms well that the quench produces the same features in the binary systems or in the Fe–S–Si system when two immiscible liquids are formed. The textural differences of the samples #2309, #412 (two immiscible Fe–S and Fe–Si liquids) and the sample #3562 (one miscible liquid) could be due to a P–T effect as shown in Fig. 5. Fig. 5 represents the data acquired by Siebert et al. (2004) and by Sanloup and Fei (2004), which obtained the first HP-HT phase diagram of the Fe–S–Si system. Even if the compositions of the present study and the ones of Siebert et al. (2004) are not exactly the same, they are all in the same range (Fe-19–23 wt%S–8–10 wt%Si alloy) and give a coherent P–T diagram. The compositions of the metallic phases in #412, #3562 and #2309 are reported in Table 3. With the two samples #412 and #2309, it is thus possible to determine the partition coefficient of Pb between Fe–S and silicate, between Fe–Si and silicate, but also between Fe–S and Fe–Si liquids.

3.2.2. Quench effects with the minor element Pb in the Fe–S alloys

Fe–Pb forms two liquids at HT and at atmospheric pressure (Moffatt, 1984). The evolution of the Fe–S–Pb phase

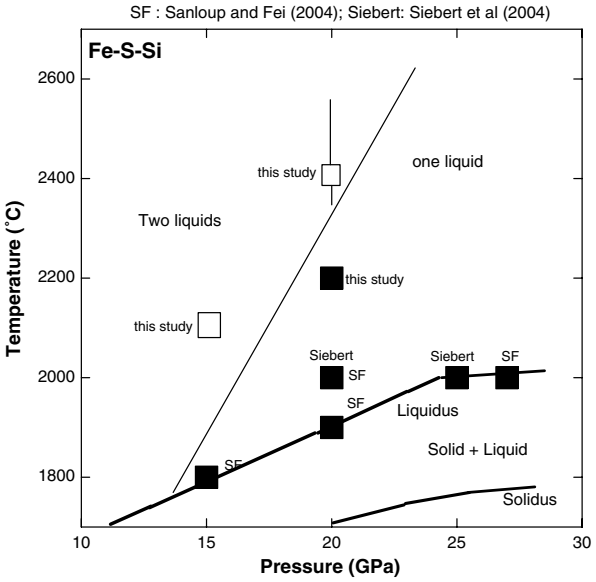

Fig. 5. Melting relations in the Fe–S–Si systems, determined by Sanloup and Fei (2004) (SF), Siebert et al. (2004) (Siebert) and by this study.

diagram is not well known at HP and HT. The Fe–S metallic phases of the present study were heterogeneous in term of Pb concentration. The major liquids were Fe–S alloys and the minor liquid was a Pb-rich alloy (Fig. 4d). This minor liquid was always observed as tiny veins embedded in the alloy matrix and never in the silicate matrix. The Fe–S metallic phases and Pb-rich alloy were always together in the whole samples. Moreover, the sizes of the two intergrown phases within metal blobs in the present samples investigated (typically 1–5 μm) (Fig. 4) are consistent with textures developing during quench (e.g. Zheng et al., 2003, 2005; Sanloup and Fei, 2004; Siebert et al., 2004). Finally, the comparison of the metallic textures between the "Fe–Si" samples and the "Fe–S" samples (Fig. 4) is relevant to show the differences between the equilibrium of two immiscible liquids and quench structures of a single HP-HT liquid. Thus, the Fe–S–Pb alloys in our samples could be a single phase at HP-HT. Because of these textures, a defocused beam (with a spot size of around 10 μm) was used with the EPMA to analyze the metallic phases, and be able to obtain the average composition of one HP-HT metallic phase. For the run #279, the μPIXE mapping gave the possibility to combine areas within a single map and allowed the determination of an average composition for the metallic phases of the sample (Table 3).

3.2.3. Immiscibility and quench effects with the minor element Pb in the Fe–Si alloys (samples #90, #92, #414, #282 and #3566)

U–Si, U–Fe and U–S are known to alloy easily at atmospheric pressure and high temperature (e.g. Moffatt, 1984). In contrast, Pb–Fe and Pb–Si do not alloy in the solid state and form generally two liquids when they are molten at atmospheric pressure (Hansen and Anderko, 1958; Moffatt, 1984). The evolution of the Fe–Si–Pb phase diagram is not well known at HP and HT. The Fe–Si metallic phases of the present study were often heterogeneous in terms of Pb concentration. The major metallic liquids were Fe–Si alloys, the minor phases were always a Pb-rich alloy (Fig. 4b and c). This Pb-rich phase was observed either as micron-scale spherical particles embedded in the alloy matrix, or as tiny rims around the metallic blob, but never in the silicate matrix. Thus, the metallic textures characterized in the recovered samples were interpreted as the result of: (1) two immiscible liquids, when the Fe–Si alloy was surrounded with Pb-rich rims (observed only in the runs #90 and #282 where the initial Pb content was the highest: 0.9 wt% for #90 and 0.5 wt% for #282), or (2) a quench effect, when micron-scale Pb-rich particles were homogeneously distributed in the Fe–Si alloy (as observed in the other samples) as already discussed in the previous paragraph above. As soon as the solubility limit of Pb in Fe–Si alloys is exceeded, Pb will form a new phase not miscible with Fe–Si, as at atmospheric pressure (e.g. Moffatt, 1984). Because of these textures, particular care was taken with the EPMA to analyze the metallic phases of #90 and #282 without the Pb-rich rims. For the run #282, the μPIXE mapping gave the possibility to easily remove this Pb contribution by directly selecting the metallic area of the sample without the Pb-rich phase (Fig. 4 and Table 3). The contribution from the Pb-rim is small because the biggest Fe–Si particles are larger than the excitation volume of the beam.

3.3. Redox conditions

It is possible to estimate the effective oxygen fugacities that have prevailed during the experiments, relative to the iron-wüstite (IW) equilibrium according to the following equation:

$$\log fO_{2\,\text{experiment}} = \log fO_{2\,\text{IW}} + 2\log(a_{FeO}/a_{Fe}) \quad (1)$$

(where a_{FeO} and a_{Fe} are respectively the activities of FeO in silicate and Fe in liquid metal, which can be defined as: $a_{FeO} = X_{Fe}^{\text{silicate}}\gamma_{Fe}^{\text{silicate}}$ and $a_{Fe} = X_{Fe}^{\text{metal}}\gamma_{Fe}^{\text{metal}}$ where γ_{Fe} is an activity coefficient). For Fe in iron rich alloys, the Raoult's law assumption generally applies (e.g. Hultgren et al., 1973); we thus assumed that the activity of Fe in the Fe–Si alloys is equal to its mole fraction when $X_{Fe} > 0.70$. The activity of Fe in the Fe–S alloys is more complicated to calculate. The assumption of ideality, that means a_{Fe} is equal to its mole fraction, had been made in previous studies (e.g. Li and Agee, 1996, 2001; Ohtani et al., 1997; Holzheid and Grove, 2002). Because of the deviation from ideality of a_{Fe}, a more appropriate fO_2 value can be obtained by using the recent results of Lee and Morita (2002) where a_{Fe} in Fe–S liquids has been calculated up to 1600 °C and for various Fe-contents. The non-ideal behavior increases with an increase in S content of the Fe–S liquid (Sharma and Chang, 1979; Hsieh et al., 1987). Finally, the difference between the ideal model and the real one is a maximum of 0.2log unit on the fO_2 of our samples. This difference is smaller than the error bar of the estimated fO_2 of our samples. These previous results, but also Waldner and Pelton (2005), show that at high

temperature Fe–S liquids approach ideality. We have calculated activity coefficients for FeO in different silicates using different sets of expressions (Fei and Saxena, 1986; Fei et al., 1991; Holzheid et al., 1997; Frost, 2003). For majorite, we used the Margules interaction parameters $W_{FeMg} = 0.3(3)$ kJ determined by Frost (2003) up to 19 GPa and 1700 °C. Because of the low FeO content of the silicates in the present study, the $\gamma_{Fe}^{majorite}$ is always close to 1 (between 1.02 and 0.99). Holzheid et al. (1997) found that the activity coefficient of FeO in silicate melt was independent of oxygen fugacity and temperature and close to unity, while several studies have indicated that the temperature dependence of the activity coefficient for pyrope-almandine garnet may be ignored (e.g. Frost et al., 2001) as the pressure dependence (Akaogi et al., 1989). The oxygen fugacities of the samples are listed in Tables 2 and 5. Application of the low P, T activity–composition relations in Fe–Si alloys (Lacaze and Sundman, 1991; Bouchard and Bale, 1995; Schlesinger and Xiang, 2001) and in Fe–S alloys leads to differences smaller than 0.4 log unit in estimated $\log fO_2$.

The partition coefficient $D_{metal–silicate}$, which is defined as the ratio of wt% in metal/wt% in silicate (which is also called the distribution coefficient), of U or Pb between metal and silicate may be described by the equations:

$$\log(D^{U}_{metal–silicate}) = A_1(T,P) - \log(\gamma^{U}_{metal}/\gamma^{U}_{silicate}) - \log fO_2 \text{ (relative to IW)} + \log C_1 \quad (2)$$

$$\log(D^{Pb}_{metal–silicate}) = A_2(T,P) - \log(\gamma^{Pb}_{metal}/\gamma^{Pb}_{silicate}) - 0.5\log fO_2 \text{(relative to IW)} + \log C_2 \quad (3)$$

where $A_{1\text{ or }2}(T,P) = -\Delta_r G(T,P)/RT$ is a parameter depending only on P and T, and $C_{1\text{ or }2}$ is a conversion factor of mole to weight ratios, and γ the activity coefficient. The Eqs. (2) and (3) predict a linear dependence of the $\log(D^{X}_{metal–silicate})$ (X represents U or Pb) with the $\log fO_2$ (relative to IW) at constant P and T and for a constant activity coefficients ratio. The theoretical slope should be −1 if the effective valence state of U is 4+ and −0.5 for Pb if the effective valence state is 2+ in the silicates.

From the analytical results of the present study, it is possible to determine the distribution coefficient $D^{X}_{metal–silicate}$ (X is Pb or U) and the exchange coefficient $K^{X}_{D\ metal–silicate}$ of Pb and U, defined as:

$$K^{X}_{d\ metal–silicate} = D^{X}_{metal–silicate}/(D^{Fe}_{metal–silicate})^{y/2} \quad (4)$$

where y is the effective valence state of X in its oxide component.

One advantage of $K^{X}_{d\ metal–silicate}$ is that, at constant pressure and temperature, this coefficient is independent of oxygen fugacity (e.g. O'Neill et al., 1998) if the effective valence state of y on its oxide component is 2. The variation of this exchange coefficient should reflect changes in the partitioning related truly to pressure and temperature.

3.4. Partitioning results

We have obtained the partition coefficients of Pb and U between silicate liquid and metal liquid at 1.5, 5 and 20 GPa, and between silicate minerals and metal liquid at 1.5, 15 and 20 GPa. As U and Pb generally partition strongly in silicate melt compared to silicate solid (e.g. Beattie, 1993; Van Westrenen et al., 1999; Corgne and Wood, 2004), care must be taken about the state of the silicate in the present study. Our partitioning results have been summarized in Table 5, Figs. 6 and 7. In Figs. 6 and 7, the distribution coefficients $D_{metal–silicate}$ of Pb (Fig. 6) and U (Fig. 7) are plotted as a function of oxygen fugacity, and the $K_{d\ metal–silicate}$ of Pb and U are also plotted as a function of pressure, temperature and the (S/Fe) ratio of the metallic phases. The theoretical linear behaviors of $D^{Pb}_{metal–silicate}$ and $D^{U}_{metal–silicate}$ with fO_2 have also been plotted.

Table 5
Distribution coefficients between metal and silicates $D_{metal/silicate}$ found in the present study at 1.5, 5, 15 and 20 GPa and between 1665 and 2400 °C

Sample		ΔIW	P (GPa)	T (°C)	Metal/silicate	$(S/Fe)_{metal}$	U	Pb
#3562	*EPMA*	−6.4	20	2200	Fe–S–Si/maj	0.36	88(±16)	22(±6)
#3563	*EPMA*	−2.2	20	2200	Fe–S/maj	0.70	0.12(±0.05)	38(±10)
#3566	*EPMA*	−3.8	20	2200	Fe–Si/maj	0	0.33(±0.08)	1.2(±0.3)
#3565	*EPMA*	−2.4	20	2200	Fe–S/maj	0.58	—	26(±8)
#2309	*EPMA*	−4.8	20	2400	Fe–S/SL	0.61	0.047(±0.020)	95(±21)
#2309	*EPMA*	−4.8	20	2400	Fe–Si/SL	0.03	0.008(±0.003)	1.2(±0.5)
#282	*EPMA*	−3.2	15	1900	Fe–Si/maj	0	0.07(±0.027)	0.63(±0.15)
#282	μ-PIXE	−3.2	15	1900	Fe–Si/maj	0	<0.10	0.86(±0.2)
#412	*EPMA*	−3.7	15	1900	Fe–S/maj	0.76	—	99(±22)
#412	*EPMA*	−3.7	15	1900	Fe–Si/maj	0.01	—	1.3(±0.3)
#279	*EPMA*	−2.9	15	1900	Fe–S/maj	0.77	0.10(±0.07)	52(±10)
#279	μ-PIXE	−2.9	15	1900	Fe–S/maj	0.77	<0.35	55(±15)
#414	*EPMA*	−5.4	5	1900	Fe–Si/SL	0	0.04 (±0.02)	1.8(±0.6)
#92	*EPMA*	−6.2	1.5	1700	Fe–Si/SL	0	—	5.6(±2)
#90	*EPMA*	−4.7	1.5	1700	Fe–Si/px	0	—	1.7(±0.6)
#96	*EPMA*	−2.3	1.5	1665	Fe–S/SL	0.60	—	14(±4)

px, pyroxene; maj, majorite; SL, silicate liquid; ML, metal liquid.

It is difficult to ignore the fact that the metallic compositions of the present study are C-saturated because all the samples, but one, were contained in a graphite capsule. We can roughly estimate the maximum C content of the metallic phases as the difference of the metal analysis total from 100%, like it was done in Chabot et al. (2005). We found that the concentrations of C in metal were always <3.5 wt%. If we used the run #414 as a "blank" for C and the Fe–C phase diagram (Okamoto, 1990) like in Chabot et al. (2006), we obtained the maximum solubility of C in metal <2 wt%. In their latest study, Chabot et al. (2006) have reported the partition coefficients $D_{\text{solid metal–liquid metal}}$ of 17 elements over a range of C contents in the Fe–Ni–C system at 1 atm. For three of the elements (Cr, Re, W), their $D_{\text{solid metal–liquid metal}}$ decreased as the C content of the metallic liquid increased. U and Pb were not studied by Chabot et al. (2006), but the modification of the behavior of the $D_{\text{solid metal–liquid metal}}$'s generally appears when the concentration of C in the metal is over 2 wt%, which does not seem to be the case in our samples. A direct comparison of our work with the results obtained by Chabot et al. (2005, 2006) is not straightforward also because the metallic compositions of these studies are quite different. The composition of the metal is an important parameter for the determination of $D_{\text{solid metal–liquid metal}}$ or $D_{\text{solid metal–liquid metal}}$. In the present study, the "C-free" sample (#414) did not show a different behavior than the other samples (obtained in C capsules). The Pb and U partition coefficients calculated from the run #414 are in good agreement with the other coefficients. At these levels of concentration, C does not seem to be a major controlling parameter of the partition coefficients of U and Pb. Its contribution may be smaller than the error made on the partition coefficients. More work is needed to better understand the real influence of C in the partitioning behavior of U and Pb.

3.4.1. Pb results

First, a striking point in these results is the apparent disagreement between the two data points obtained by Ohtani et al. (1997) and Ohtani and Yurimoto (1996) on the one hand, and this study on the other (Fig. 5). After a careful look at their studies, we think that this difference might be due to the differences in the starting metallic compositions. A mixture of 1 wt% of each V, Cr, Mn, Co, Ni, P, Mo, Pt, Re, W and 90 wt% of Fe was used as starting metallic phase. New Pb thermodynamical behavior could be promoted by one of the elements added as dopants. Since all of the elements of interest are known to interact with one another in metallic liquids (J.S.f.t.P.o. S.a.T.t.C.o. Steelmaking, 1988; Wade and Wood, 2005), partitioning experiments performed under different compositional conditions are bound to produce scattered results. This could be a first explanation about this discrepancy. No Pb was directly added in their experiments, thus Pb came from the natural peridotite mixed with the metal. Another difference comes from the relatively high Pb concentrations in the metallic phases (between 7 wt% and 900 ppm) of the present work compared to those found in Ohtani et al. (1997) and Ohtani and Yurimoto (1996) (134 and 88 ppm). Thus, we can not exclude the possibility that Henry's law is violated in our samples. A simple way to check to the Henry's law validity domain is given by the Fig. 8. The Fig. 8 shows the concentrations of Pb in Fe–Si alloys plotted against the concentration of Pb in majorite. For experiments performed under the same P–T redox conditions, and if the data can be fitted by straight lines through the origin, therefore the data are consistent with Henry's law. This is the case for the two data that can be plotted in such diagrams. On the other hand, our results are in agreement with the results of Jones (1995). In the Fig. 6d, where the evolution of $K^{\text{Pb}}_{\text{metal–silicate}}$ is plotted vs the S/Fe ration of the metallic phases, one sample is out of the major trend given by the other samples. This is the sample #3562 (20 GPa–2200 °C) where a homogeneous Fe–S–Si metallic liquid was in equilibrium with the silicates. This is the only sample which contains Si and S together its $K^{\text{Pb}}_{\text{metal–silicate}}$ is lower than the others obtained just from the binary Fe–S or Fe–Si. Maybe, this lower $K^{\text{Pb}}_{\text{metal–silicate}}$ could be related to a compositional effect due to the metallic phase. For example, the activity of Si in the 63.6 wt%Fe–8.6 wt%Si–23.3 wt%S alloy could change compared to alloys containing around 0.1 and 1.5 wt% of Si and more than 35 wt% of S, because a strong non-ideal behavior is already observed for Si in the Fe–Si system.

The largest controlling factors of these partition coefficients seem to be the redox conditions (Fig. 6) and the metallic composition. The partition coefficients obtained with the Fe–S metallic phases are higher (that means always siderophile) than those obtained with Fe–Si alloys. Pressure (P) and temperature (T) do not seem to significantly affect $K^{\text{Pb}}_{\text{metal–silicate}}$ (Fig. 6) but more data are still needed to confirm this. The $D^{\text{Pb}}_{\text{metal–silicate}}$'s show a fO_2 dependence (Fig. 6) which follows the theoretical −0.5 slope, implying a valence state of 2 for Pb in the silicates minerals (pyroxene or majorite) or liquid as expected. The change in the mineral, pyroxene or majorite, does not affect a lot the partition coefficient as well. The metallic composition (particularly the S content of the metal) seems to be also a major parameter for the evolution of $K^{\text{Pb}}_{\text{metal–silicate}}$.

An average difference of 0.55log unit is observed between the partition coefficient between metal/majorite and between silicate liquid/metal. This value could be compared to the distribution coefficients $D^{\text{Maj/Melt}}$ of Pb between majorite and silicate melt leading to a value of 0.25 ± 0.20 from our work. Corgne and Wood (2004) found a $D^{\text{Maj/Melt}}$ of 0.13 ± 0.2 at 25 GPa and 2300 °C. Regarding the differences of compositions, P, T and fO_2, the $D^{\text{Maj/Melt}}$ deduced from our graphs is coherent with the result of Corgne and Wood (2004). Finally, our data confirms the well known incompatible trend of Pb.

We obtained no correlation with diagrams, which represented $D^{\text{Pb}}_{\text{metal–silicate}}$ as a function of nbo/t (which is the molar ratio of nonbridging oxygens to tetrahedrally coordinated cations, Mysen and Virgo, 1980) of the silicates. nbo/t is used often as a characteristic parameter of the silicate composition (e.g. Jana and Walker, 1997). To be able to visualize the real influence of this parameter, we need to have more data: at one T and P for different nbo/t.

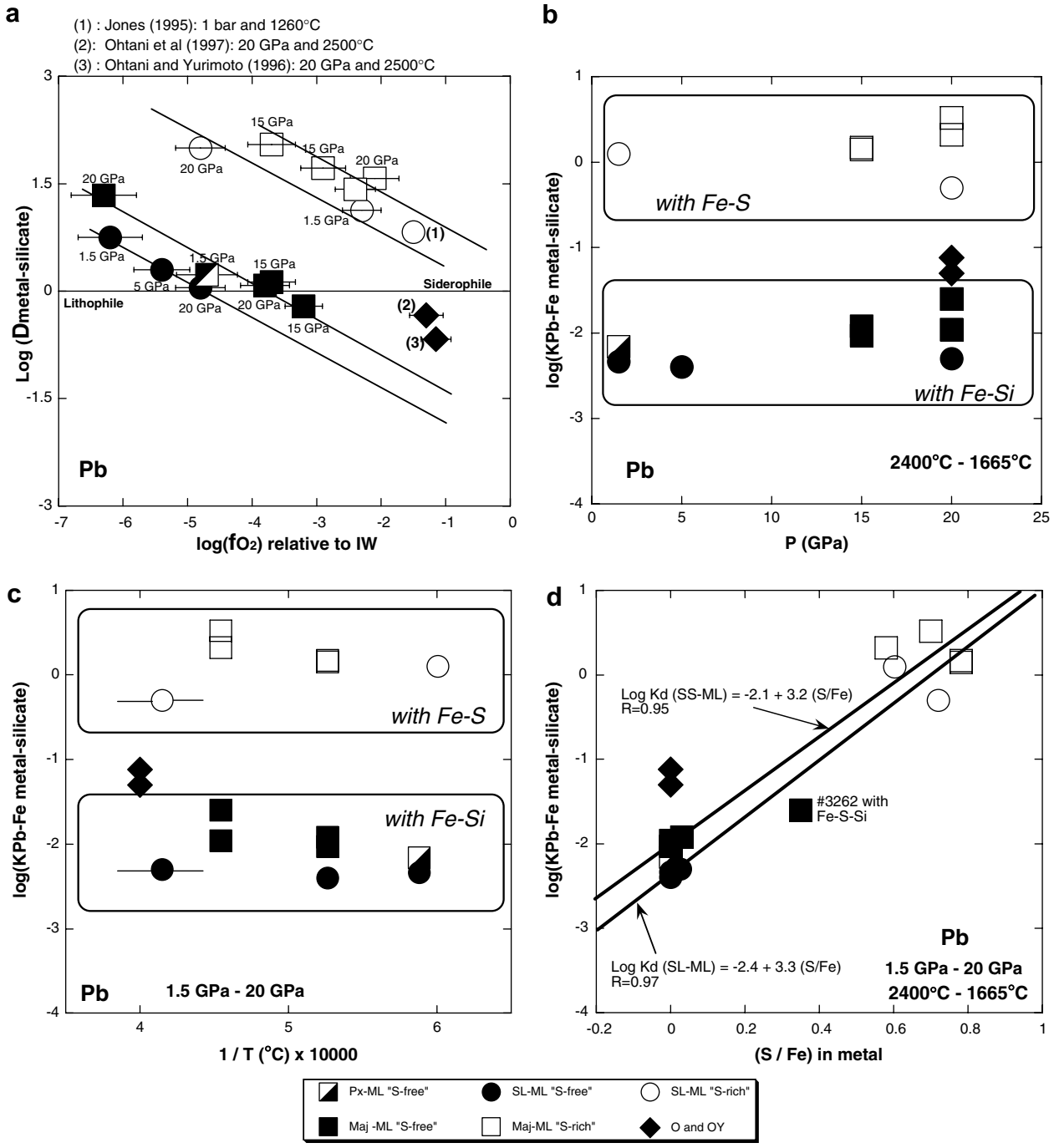

Fig. 6. The experimental partition coefficients for Pb between metal and silicate are plotted vs (a) fO_2 relative to IW at different pressures. Summary of experimental results of this study for Pb and previous work by Jones (1995) at 1 bar and 1260 °C, Ohtani and Yurimoto (1996) at 20 GPa and 2500 °C, Ohtani et al. (1997) at 20 GPa and 2500 °C. All filled symbols represent a system where either Fe–Si alloys are the metallic phases or pure Fe. All the empty symbols represent a chemical system where S is present in the metal. All square symbols are for Pb partition coefficients between silicate mineral (pyroxene (px) half-full square symbols, or majorite (maj) full square symbols) and metal liquid (ML); all round symbols are for the partition coefficients between silicate liquid (SL) and metal liquid. (b) Exchange coefficients versus pressure (c), temperature (d) and versus the (S/Fe) of the metallic phase. The symbol size represents the error.

3.4.2. U results

As already reported by Wheeler et al. (2006), the largest controlling factors of these partition coefficients seem to be the metallic composition, but also the redox conditions (Fig. 7). From Fig. 7 where the $K^{U}_{metal–silicate}$'s are plotted vs P or T, it is clear that the $K^{U}_{metal–silicate}$'s show no discernable P or T trend. To the contrary, the $D^{U}_{metal–silicate}$'s show a fO_2 dependence (Fig. 7) which follows the theoretical −1

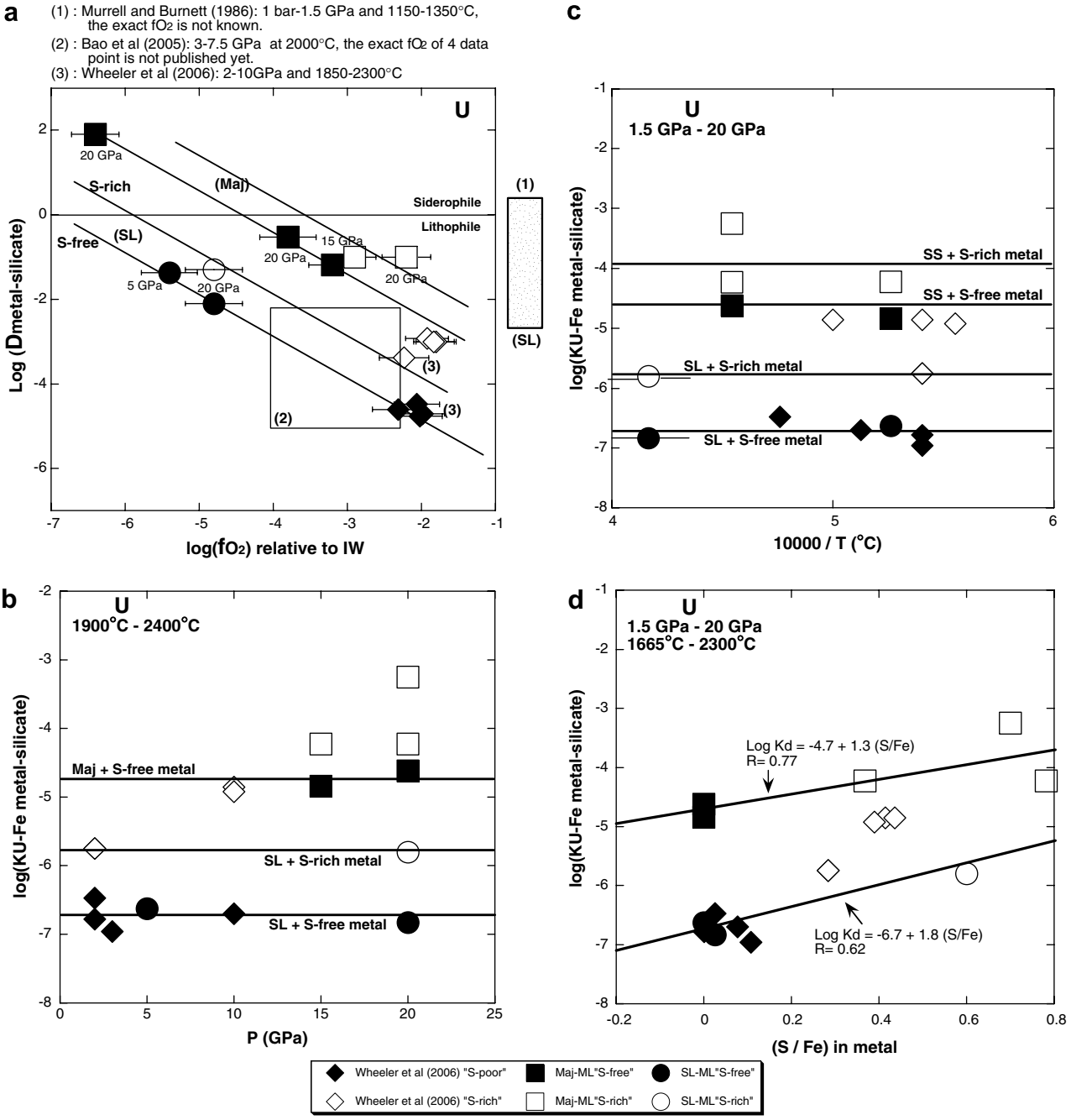

Fig. 7. The experimental partition coefficients for U between metal and silicate are plotted vs (a) fO_2 relative to IW at different pressures. Summary of experimental results of this study for U and previous work by Wheeler et al. (2006), Murrell and Burnett (1986) at 1 bar - 1.5 GPa and 1150–1450 °C, and Bao et al. (2005) at 3–7.5 GPa and 1900–2000 °C. All filled symbols represent a system where either Fe–Si alloys are the metallic phases or pure Fe. All the empty symbols represent a chemical system where S is present in the metal. All square symbols are for Pb partition coefficients between majorite and metallic liquid (ML) square symbols; all round symbols are for the partition coefficients between silicate liquid (SL) and metal liquid. Exchange coefficients versus pressure (b), temperature (c), and versus the (S/Fe) of the metallic phase (c), and versus the S/Fe ratio of the metallic phases (d). The symbol size represents the error.

slope, implying a valence state of 4 for U in the silicates solid or liquid. All the piston cylinder experiments of Wheeler et al. (2006) ranging from 1 to 3 GPa and 2300–1750 °C are in very good agreement with our data obtained from silicate liquid–metal liquid. The discrepancy with three 10 GPa runs of Wheeler et al. (2006) could: (i) reflect the difficulties of measuring so small amount of U in metal and could show the characteristic interval of the error made on D^U, (ii) be due to the fact that Wheeler et al. (2006) began their experiments with native U while we began ours with UO_2,

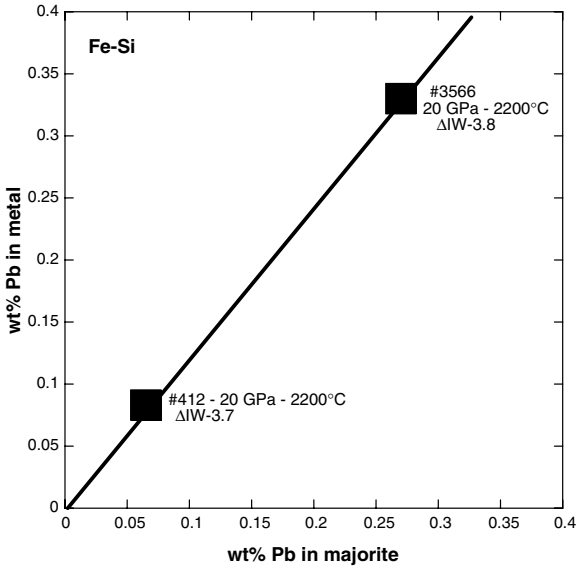

Fig. 8. The concentrations of Pb in Fe–Si plotted against the concentration of Pb in majorite in samples #3566 and #412. For these two experiments performed under the same P–T redox conditions (20 GPa, 2200 °C, ΔIW-3.8/-3.7), and if the data can be fitted by straight line through the origin, therefore the data are consistent with Henry's law. The symbol size represents the error.

(iii) be due to the fact that the KLB-1 silicate of these 10 GPa samples might not be totally molten as their P–T conditions (10 GPa and T ranging between 1800 and 2000 °C) are very close to the KLB-1 liquidus found (10 GPa–2100 °C) by Zhang and Herzberg (1994) and Herzberg and Zhang (1996).

An average difference of 2.4 log unit is observed between the partition coefficient between majorite/metal liquid and between silicate liquid/metal liquid. This value could be compared to the distribution coefficients $D^{\mathrm{Maj/Melt}}$ of U between mineral and silicate melt leading to a value of 0.004 ± 0.002 from our work. Corgne and Wood (2004) found a $D^{\mathrm{Maj/Melt}}$ of 0.02 ± 0.005 at 25 GPa and 2300 °C. This value is very close to that one found by Van Westrenen et al. (1999) at lower pressure (3 GPa) and temperature (up to 1565 °C). Regardless the differences of compositions, P, T and fO_2, the $D^{\mathrm{Maj/Melt}}$ deduced from the Fig. 7 is coherent with the results of Corgne and Wood (2004) and Van Westrenen et al. (1999). The strong incompatible trend of U is thus shown by our data. Our results confirm the higher incompatible trend of U compared to Pb.

4. DISCUSSION

A direct comparison with previous studies is not straightforward because partition coefficients depend on the composition of the silicates and metals and redox conditions. In particular, the comparison with the $D^{\mathrm{U}}_{\mathrm{met-sil}}$ of Murrell and Burnett (1986) is very difficult since these authors did not give the real fO_2 of their experiments. Their values for $D^{\mathrm{U}}_{\mathrm{met-sil}}$ were between 0.002 and 2, over the temperature range 1150–1350 °C and the pressure range 1 bar–15 kbars. These authors emphasized that U became less lithophile under low oxygen fugacity. The present study confirmed these first experimental observations

4.1. The first terrestrial isotope paradox and the Earth's core heat flux

We made the assumption that a HP-HT-core-mantle equilibrium have been reached on Earth during the core segregation process around ΔIW-2 (e.g. Chabot and Agee, 2003; Chabot et al., 2005; Wade and Wood, 2005). From the $D_{\mathrm{metal-silicate}}$ of the present study and U and Pb contents of the mantle (values are given in Tables 6 and 7) we obtained: $0.008\ \mathrm{ppm} < \mathrm{Pb}_{\mathrm{in\ the\ core}} < 4.4\ \mathrm{ppm}$, and $0.0003\ \mathrm{ppb} < \mathrm{U}_{\mathrm{in\ the\ core}} < 0.63\ \mathrm{ppb}$, depending on whether the metal is S-free or S-rich respectively. The heat flow from the core to the mantle is estimated around 7 TW for the present time value, whereas it was as high as 8 TW when the inner core initiated solidification (e.g. Yukutake, 2000; Labrosse, 2003). To supply 7 TW, the U core concentration currently required, exclusive of any other heat source, is about 40 ppb of U. With the same reasoning, we found that around 50 ppb of U is needed to supply 8 TW. Thus, the range of U concentration in the core found here represents a negligible contribution of the heat flow from the core to the mantle.

If we suppose that all the Pb missing in the Earth's mantle is sequestered in the core, with a simple mass balance calculation and the assumption of an initial CI chondritic content of Pb on Earth, we find that a maximum of 7.5 ppm of Pb should be in the core. As 7.5 ppm >4.4 ppm, we can conclude that a Pb sequestration in the core can not readily explain the first terrestrial Pb paradox, and this even if the core was S-saturated (which represents an unreachable upper limit of Pb in the core, 4.4 ppm).

How did these U and Pb limits evolve, if the fO_2 varied during the differentiation process (e.g. Wänke et al., 1984; Javoy, 1995; Chabot et al., 2005; Wade and Wood, 2005)? New constraints could come from our $K^{\mathrm{Pb}}_{\mathrm{metal-silicate}}$ and $K^{\mathrm{U}}_{\mathrm{metal-silicate}}$ data. The ratio $K^{\mathrm{U}}/K^{\mathrm{Pb}}$ is less dependent on the oxygen fugacity compared to the ratio of the distribution coefficients $D^{\mathrm{Pb}}_{\mathrm{met-sil}}$. $K^{\mathrm{U}}_{\mathrm{met-sil}}$ and $K^{\mathrm{Pb}}_{\mathrm{metal-silicate}}$ have no discernable P or T trend, giving us the possibility to use them directly as:

$$(\mathrm{U/Pb})_{\mathrm{core}} = (K^{\mathrm{U}}/K^{\mathrm{Pb}})(\mathrm{U/Pb})_{\mathrm{mantle}}(\mathrm{Fe_{core}/Fe_{mantle}}) \qquad (5)$$

with $(\mathrm{U/Pb})_{\mathrm{mantle}}$ being the ratio of the U and Pb concentrations of the mantle and $(\mathrm{Fe_{core}/Fe_{mantle}})$ the ration of the Fe content of the core and the Fe concentration of the mantle (cf. Table 7). As we have a first estimation of the evolution of $K^{\mathrm{U}}_{\mathrm{metal-silicate}}$ and $K^{\mathrm{Pb}}_{\mathrm{metal-silicate}}$ as a function of the (S/Fe) ratio of the metallic phase (Figs. 5 and 6), it is thus possible to calculate (4) as a function of the (S/Fe) ratio of the core. If we suppose that 7.5 ppm of Pb are in the core, then from (4), the maximum U content of the core constrained with geochemical models could be calculated. From these maximum values of U and the evolution of D^{U} with fO_2, the minimum required fO_2's prevailing during the core formation could be deduced. They are in the following range: ΔIW-5.5 <log(fO_2) relative to IW <ΔIW-3, depending on the S content of the metallic phase and the

Table 6
Distribution coefficients used to constrain the U and Pb contents in the Earth's core at ΔIW-2 and in the Martian core at ΔIW-1

	Pb	U	fO_2 relative to IW
Fe–S/majorite	24 ± 10	0.03 ± 0.02	ΔIW-2
Fe–S/Silicate Liquid	6.3 ± 3	0.00014 ± 0.00007	ΔIW-2
Fe–Si/majorite	0.13 ± 1	0.0044 ± 0.02	ΔIW-2
Fe–Si/Silicate Liquid	0.042 ± 0.02	0.000014 ± 0.00007	ΔIW-2
Fe–S/majorite	7.6 ± 4	0.003 ± 0.002	ΔIW-1
Fe–S/Silicate Liquid	2 ± 1	0.000014 ± 0.00001	ΔIW-1
Fe–Si/majorite	0.042 ± 0.02	0.00044 ± 0.002	ΔIW-1
Fe–Si/Silicate Liquid	0.014 ± 0.007	$0.0000014 \pm .00001$	ΔIW-1

These coefficients have been calculated with the Figs. 5 and 6 and assuming a theoretical trend (which means a slope of −1 for U and −0.5 for Pb in the $\log D_{\text{metal–silicate}}$ *vs.* ΔIW diagram).

Table 7
Values used here to constrain the U and Pb concentrations in the Earth's and Martian cores

Abundances in the mantle	References	Abundances in the core	References
Earth–Pb: 0.185 ppm	Palme and O'Neill (2003)	Earth–S: 1.9 wt%	McDonough (2003)
Earth–Pb: 0.175 ppm	Hofmann (1988)	Earth–S: 2.3 wt%	Allègre et al. (1995)
Mars–Pb: 0.366 ppm	Dreibus and Jagoutz (2002)	Mars– S: 10.6 wt%	Lodders and Fegley (1997)
Mars–Pb: 0.38 ppm	Lodders and Fegley (1997)	Mars–S: 14.2 wt%	Wänke and Dreibus (1994)
Earth–U: 21.9 ppb	Palme and O'Neill (2003)	Earth–Fe: 79 wt%	Allègre et al. (1995)
Earth–U: 21 ppb	Longhi et al. (1992)	Earth–Fe: 85.5 wt%	McDonough (2003)
Mars–U: 16 ppb	Lodders and Fegley (1997)		
Mars–U: 16 ppb	Longhi et al. (1992)		
Earth–Fe: 5.82 wt%	Allègre et al. (1995)		
Earth–Fe: 6.3 wt%	Palme and O'Neill (2003)		
Earth–Fe: 6.26 wt%	McDonough (2003)		
Mars–Fe: 13.38 wt%	Lodders and Fegley (1997)		
Mars–Fe: 13.9 wt%	Wänke and Dreibus (1994)		

state of the silicates. With a magma ocean occurring during the Earth's accretion, a maximum of 1.5% of the total heat budget of the core might be produced by the decay of U and being in agreement with an early incorporation of Pb in a Fe–S core. The interesting point here is to show how the redox conditions prevailing over the core formation could be a crucial parameter to enter or not some U in the core, as well as the state of the silicates (molten or solid). With a magma ocean scenario, very reduced conditions (at least $\Delta IW < -4.5$) must take place to enter significant amount of U in the core. Such reduced conditions are in disagreement with all the other models of core formation, which are based on siderophile elements partitioning (Chabot et al., 2005; Wade and Wood, 2005). Thus, we can conclude that the content of U in the core represents a negligeable contribution of the heat flow from the core to the mantle.

Finally, the latest ideas suggested by Wood and Halliday (2005) could be another way to introduce massively some Pb in the core. They proposed that after the Moon-forming-giant impact a late segregation of an extremely small volume (<1%) sulphur-rich metal appeared giving a way for Pb to go away readily from the mantle. This scenario of accretion would imply that this particular Fe–S segregation might take place above ΔIW-2. If we use our Pb results to constraint the theory of Wood and Halliday (2005), we see that above ΔIW-2 it might be difficult to obtain a strong concentration of Pb in a S-rich metal. For example, if we want to solve the Pb paradox with this scenario (a late segregation of Fe–S through a molten mantle), that would imply between 800 and 50 ppm of Pb in this Fe–S metal (depending mainly on the exact proportion of this phase in the core) implying redox conditions below ΔIW-5. This condition is incompatible with the required scenario of Wood and Halliday (2005).

In future, new experiments should be done in order to quantify precisely the evolution of $D^{Pb}_{\text{metal–silicate}}$, $D^{U}_{\text{metal–silicate}}$, $K^{U}_{\text{metal–silicate}}$ and $K^{Pb}_{\text{metal–silicate}}$ with different S content in the metallic phase, and more work are still needed at HP-HT where the Fe–S–Si miscibility gap is closed.

4.2. The martian core and its magnetic field

The knowledge of Mars interior is principally based on interpretation of gravity data, on analyses of SNC meteorites, on extrapolation of the Earth's internal structure to the lower pressures of the internal structure of Mars and on the observational determination of the precession constant from Viking and Pathfinder (Folkner et al., 1997). The mass of the core compatible with these measurements is from 14 to 22 wt% of the total mass of Mars. From recent results (e.g. Lodders and Fegley, 1997; Fei and Bertka, 2005; Fei et al., 2006), one concludes that the Martian core might be entirely liquid. We made the assumption that a HP-HT-core-mantle equilibrium has been reached on Mars during

the core segregation process around ΔIW-1 based on the iron content of the martien mantle (Rubie et al., 2004). From the $D_{metal-silicate}$ of the present study and the U and Pb content of the mantle (values are given in Tables 6 and 7), we obtained that: 0.005 ppm $< Pb_{in\ the\ core} <$ 3 ppm, and 0.00002 ppb $< U_{in\ the\ core} <$ 0.05 ppb, depending on the metallic composition: S-free or S-rich respectively.

Mars has no modern internal magnetic field of global extent. Mars is thought to have possessed a dynamo that ceased around 0.5 b.y. after its formation (Williams and Nimmo, 2004). A magnetic field generated internally by dynamo activity in the core requires core convection, a condition that is most likely to be met when the heat flux from the core into the mantle exceeds the critical amount that is estimated to be 5–19 mW/m^2 (Nimmo and Stevenson, 2000). Our results suggest that if the Martian core was heated mainly by U during its early magnetic field history, Pb might have been massively incorporated into a Fe–S core during a segregation process but only with a S-rich core. In contrast, a S-free core formation process through a mantle (molten or solid) led a loss of Pb from the mantle possible by a light incorporation in the core and also by volatility as already suggested by Dreibus and Jagoutz (2002). Anyway, the upper limits of fO_2 required to heat the Martian core only with U should be very low compared to the likely present redox of the Martian mantle. This could simply imply that the magnetic field activity of Mars before ~0.5 b.y. after its formation could not be ascribed at the decay of U alone.

ACKNOWLEDGMENTS

The lowest pressure (5 and 15 GPa) multi-anvils experiments were performed using a 1000-tonne multianvil apparatus at the "Laboratoire Volcan et Magma", Clermont-Ferrand (France), under the French national facility of INSU. The highest pressure (20 GPa) multi-anvils experiments were performed using a 1200-tonne multianvil apparatus at the Bayerisches Geoinstitut under the EU "Research Infrastructures: Transnational access" Programme (Contract No. 505320 RITA High Pressure). The micro-PIXE analysis have been performed in the laboratoire Pierre Süe (France) under the French facility of INSU. We would like to thank Ali Bouhifd who gave the glass used as starting compositions for several experiments in this study, Don Musselwhite, Dan Frost and Nathalie Bolfan for their precious assistance with high-pressure experiments and Michel Fialin for his help and assistance with the EPMA in Paris. This project was partly funded by the 2004 French National program DyETI. We appreciate the thoughtful and thorough reviews of Liz Cottrell and two anonymous reviewers, which helped to improve the final manuscript. Finally, VM would like to add a special thank to Loan Lee for her precious help in the lab in Houston, her patience and her kindness during the two years spent there. This is the LPI contribution #1296.

REFERENCES

Allègre C. J. (1982) Chemical geodynamics. *Tectonophysics* **81**, 109–132.

Allègre C., Poirier J. P., Humler E., and Hofman A. (1995) The chemical composition of the earth. *Earth Planet. Sci. Lett.* **134**, 515–526.

Allègre C., Manhès G., and Lewin E. (2001) Chemical composition of the earth and the volatility control on planetary genetics. *Earth Planet. Sci. Lett.* **185**, 49–69.

Akaogi M., Ito E., and Navrosky A. (1989) The olivine-modified spinel-spinel transitions in the system Mg_2SiO_4–Fe_2SiO_4: calorimetric measurements, thermochemical calculation, and geophysical application. *J. Geophys. Res.* **94**, 15671–15686.

Bao X., Secco R. A., Gagnon J. E., and Fryer B. J. (2005) Experiments of U Solubility in Earth's Core. *Eos Trans. AGU* **86(18)**, Jt. Assem. Suppl., (abstr.).

Beattie P. (1993) Uranium-thorium disequilibria and partitioning on melting of garnet peridotite. *Nature* **363**, 63–65.

Bouchard D., and Bale C. W. (1995) Ti-Si Interaction in liquid iron. *Can. Metall. Q.* **34**, 343–346.

Bouhifd M. A., and Jephcoat A. P. (2003) The effect of pressure on partitioning of Ni and Co between silicate and iron-rich metal liquids: a diamond-anvil cell study. *Earth Planet. Sci. Lett.* **209**, 245–255.

Bouhifd M. A., Gautron L., Bolfan-Casanova N., Malavergne V., Hammouda T., Andrault D., and Jephcoat A. P. (2007) Potassium partitioning into molten iron alloys at high-pressure: Implications for Earth's core. *Phys. Earth Planet. Int* **160**, 22–33.

Buffett B. A. (2000) Earth's core and the geodynamo. *Science* **288**, 2007–2012.

Chabot N. L., and Drake M. J. (1999) Potassium solubility in metal: the effects of composition at 15 kbar and 1900 °C on partitioning between iron alloys and silicate melts. *Earth Planet Sci. Lett.* **172**, 323–335.

Chabot N. L., and Agee C. B. (2003) Core formation in the Earth and Moon: New experimental constraints from V, Cr, and Mn. *Geochim. Cosmochim. Acta* **67**, 2077–2091.

Chabot N. L., Draper D. S., and Agee C. B. (2005) Conditions of core formation in the Earth: constraints from nickel and cobalt partitioning. *Geochim. Cosmochim. Acta* **69**, 2141–2151.

Chabot N. L., Campbell A. J., Jones J. H., Humayun M., and Vern Lauer, Jr., H. (2006) The influence of carbon on trace element partitioning behavior. *Geochim. Cosmochim. Acta* **70**, 1322–1335.

Cherniak D. J. (1998) Pb diffusion in clinopyroxene. *Chem. Geol.* **150**, 105–117.

Corgne A., and Wood B. (2004) Trace element partitioning between majoritic garnet and silicate melt at 25 GPa. *Phys. Earth Planet. Int.* **144**, 407–419.

Daudin L., Khodja H., and Gallien J. P. (2003) Development of position–charge–time" tagged spectrometry for ion beam microanalysis. *Nucl. Instrum. Meth. B* **210**, 153–158.

Dreibus G., and Jagoutz E. (2002) Radiogenic isotopes and bulk composition of Mars, In *Lunar Planet. Sci. Conf. XXXIII*. Abstract #1040, Lunar and Planetary Institute, Houston (CD-ROM).

Feber R. C., Wallace T. C., and Libby L. M. (1984) Uranium in the Earth's core. *Eos Trans. AGU* **65**, 785.

Fei Y., and Saxena S. (1986) A thermochemical data base for phase equilibra in the system Fe_Mg_Si_O at high pressure and temperature. *Phys. Chem. Miner.* **13**, 311.

Fei Y., Mao H-K., and Mysen B. (1991) Experimental determination of element partitioning and calculation of phase relation in the MgO–FeO–SiO_2 system at high pressure and high temperature. *J. Geophys. Res.* **96**, 2157–2169.

Fei Y., Bertka C. M., and Finger L. W. (1997) High-pressure iron–sulfur compound, Fe_3S_2, and melting relations in the system Fe–FeS at high pressure. *Science* **275**, 1621–1624.

Fei Y., Li J., Bertka C. M., and Prewitt C. T. (2000) Structure type and bulk modulus of Fe_3S, a new iron–sulfur compound. *Am. Mineral.* **85**, 1830–1833.

Fei Y., and Bertka C. M. (2005) The interior of Mars. *Science* **308**, 1120–1122.

Fei Y., Zhang L., Komabayashi T., Sata N., and Bertka C. M. (2006) Evidence for a liquid martian core. In *Proc. 11th Lunar Planet. Sci. Conf. XXXVII*. Abstract #1500.

Fialin M., Rémy H., Richard C., and Wagner C. (1999) Trace element analysis with the electron microprobe: new data and perspectives. *Am. Mineral.* **84**, 70–77.

Folkner W. M., Kahn R. D., Preston R. A., Yoder C. F., Standish E. M., Williams J. G., Edwards C. D., and Hellings R. W. (1997) Mars dynamics from Earth-based tracking of Mars Pathfinder lander. *J. Geophys. Res.* **102**, 4057–4064.

Frost D. J., Langenhorst F., and van Aken P. A. (2001) Fe-Mg partitioning between ringwoodite and magnesiowüstite and the effect of pressure, temperature and oxygen fugacity. *Phys. Chem. Miner.* **28**, 455–470.

Frost D. J. (2003) Fe^{2+}–Mg partitioning between garnet, magnesiowüstite and (Mg, Fe)$_2SiO_4$ phases of the transition zone. *Am. Miner.* **88**, 387–397.

Furst M. J., Stapanian M. I., and Burnett D. S. (1982) Observation of non-lithophile behavior for U. *Geophys. Res. Lett.* **9**, 41–44.

Gasparik T. (2000) Evidence for immiscibility in the majorite garnet from experiments at 13–15 GPa. *Geochim. Cosmoschim. Acta* **64**, 1641–1650.

Gasparik T. (2003) *Phase Diagrams for Geoscientists*. Springer, Berlin, Heiderlberg, New York.

Gillet P., Fiquet G., Malezieux J. M., and Geiger C. A. (1992) High-pressure and high- temperature Raman spectroscopy of end-member garnets: pyrope, grossular and andradite. *Eur. J. Mineral.* **4**, 651–664.

Gessmann C. K., and Rubie D. C. (1998) The effect of temperature on the partitioning of nickel, cobalt, manganese, chromium, and vanadium at 9 GPa and constraints on formation of the Earth's core. *Geoch. Cosmoschim. Acta* **62**, 867.

Gessmann C. K., and Rubie D. C. (2000) The origin of the depletion of V, Cr and Mn in the mantles of the Earth and Moon. *Earth Planet. Sci. Lett.* **184**, 95–107.

Gessmann C. K., and Wood B. J. (2002) Potassium in the Earth's core?. *Earth Planet. Sci. Lett.* **200** 63–78.

Gubbins D., Masters T. G., and Jacobs J. A. (1979) Thermal evolution of the Earth's core. *Geophys. J. R. Astron. Soc.* **59**, 57–99.

Gudkova T. V., and Zharkov V. N. (2004) Mars: interior structure and excitation of free oscillations. *Phys. Earth Planet. Int.* **142**, 1–22.

Hammouda T. (2003) High-pressure melting or carbonated eclogite and experimental constraints on carbon recycling and storage in the mantle. *Earth Planet. Sci. Lett.* **214**, 357–368.

Hansen M., and Anderko K. (1958) *Constitution of binary alloys*, Second edition. McGraw-Hill book company.

Herzberg C., and Zhang J. (1996) Melting experiments on anhydrous peridotite KLB-1: compositions of magmas in the upper mantle and transition zone. *J. Geophys. Res.* **101**, 8271–8295.

Hirao N., Ohtani E., Kondo T., Endo N., Kuba T., Suzuki T., and Kikegawa T. (2006) Partitioning of potassium between iron and silicate at the core-mantle boundary. *Geophys. Res. Lett.* **33**, L08303. doi:10.1029/2005GL02532.

Hofmann A. W. (1988) Chemical differentiation of the earth: the relationship between mantle, continental crust, and oceanic crust. *Earth Planet. Sci. Lett.* **90**, 297–314.

Holzheid A., Palme H., and Chakraborty S. (1997) The activities of NiO, CoO and FeO in silicate melts. *Chem. Geol.* **139**, 21–38.

Holzheid A., and Grove T. (2002) Sulfur saturation limits in silicate melts and their implications for core formation scenarios for terrestrial planets. *Am. Mineral.* **87**, 227–237.

Hsieh K. C., Vlach K. C., and Chang Y. A. (1987) The Fe–Ni–S system I. A thermodynamic analysis of the phase equilibria and calculation of the phase diagram from 1173 K to 1623 K. *High Temp. Sci.* **23**, 17–38.

Hultgren R., Desai P. D., Hawkins D. T., Gleiser M., and Kelley K. K. (1973) *in Selected values of the thermodynamic properties of binary alloys*. American Society for Metals, Metals Park, Ohio, 1435 p.

Ito E., Morooka K., and Ujike O. (1993) Dissolution of K in molten iron at high pressure and temperature. *Geophys. Res. Lett.* **20**, 1651–1654.

Ito E., Kubo A., Katsura T., and Walter M. J. (2004) Melting experiments of mantle materials under lower mantle conditions with implications for magma ocean differentiation. *Phys. Earth Planet. Int.*, 397–406.

Jana D., and Walker D. (1997) The influence of silicate melt composition on distribution of siderophile elements among metal and silicate liquids. *Earth Planet Sci. Lett.* **150**, 463–472.

Javoy M. (1995) The integral enstatite chondrite model of the Earth. *Geophys. Res. Lett.* **22**, 2219–2222.

Jones J. H., and Drake M. J. (1986) Geochemical constraints on core formation. *Nature* **322**, 221–228.

Jones, J. (1995) Experimental trace element partitioning, *Rock Physics and Phase Relations: A Handbook of Physical Constants, AGU Reference Shelf*, vol. 3 (ed. T. J. Ahrens). American Geophysical Union, Washington, DC, pp. 73–104.

J.S.f.t.P.o.S.a.T.t.C.o. Steelmaking. (1988) *Steelmaking Data Sourcebook*, Gordon and Breach Science Publishers, Montreux.

Karato S. I., and Murthy V. R. (1997) Core formation and chemical equilibrium in the Earth: I Physical considerations. *Phys. Earth Planet. Int.* **100**, 61–79.

Khodja H., Berthoumieux E., Daudin L., and Gallien J. P. (2001) The Pierre Süe Laboratory nuclear microprobe as a multidisciplinary analysis tool. *Nucl. Inst. Meth. B* **181**, 83–86.

Kokubo E., and Ida S. (2000) Formation of protoplanets from planetesimals in the solar nebula. *Icarus* **143**, 15–27.

Kramers J. D., and Tolstikhin I. N. (1997) Two terrestrial lead isotope paradoxes, forward transport modeling, core formation and the history of the continental crust. *Chem. Geol.* **139**, 75–110.

Kuwayama Y., and Hirose K. (2004) Phase relation in the system Fe–FeSi at 21 GPa. *Am. Mineral.* **89**, 273–276.

Labrosse S., Poirier J. P., and Le Mouël J. L. (2001) The age of the inner core. *Earth Planet. Sci. Lett.* **190**, 111–123.

Labrosse S. (2003) Hotspots, mantle plumes and core heat loss. *Phys. Earth Planet. Int.* **140**, 127–143.

Lacaze J., and Sundman B. (1991) An assessment of the Fe–C–Si system. *Metall. Trans. A* **22A**, 2211–2223.

Lee K. K. M., and Jeanloz R. (2003) High-pressure alloying of potassium and iron: radioactivity in the Earth's core? *Geophys. Res. Lett.* **30**, 2212. doi:10.1029/2003GL01851.

Lee J., and Morita K. (2002) Evaluation of surface tension and adsorption for liquid Fe–S alloys. *ISIJ Int.* **42**, 588–594.

Li J., and Agee C. B. (1996) Geochemistry of mantle-core differentiation at high pressure. *Nature* **381**, 686–689.

Li J., and Agee C. B. (2001) The effect of pressure, temperature, oxygen fugacity and composition of nickel and cobalt between liquid Fe–Ni–S alloy and liquid silicate: implications for the Earth's core formation. *Geochim. Cosmochim. Acta* **65**, 1821–1832.

Li J., Hadidiacos C., Mao H. K., Fei Y., and Hemley R. (2003) Behaviour of thermocouples under high pressure in multi-anvil apparatus. *Int. J. High Press. Res.* **23**, 389–401.

Lodders K., and Fegley, Jr., B. (1997) An oxygen isotope model for the composition of Mars. *Icarus* **126**, 373–394.

Longhi J., Knittle E., Holloway J.R., and Wänke H. (1992) The bulk composition, mineralogy and internal structure of Mars.

In *Mars* (eds. H.H. Kieffer, B.M. Jakowsky, C.W. Snyder and M.S. Matthews), Univ. Arizona Press, Tucson, pp. 184–208.

Malavergne V., Siebert J., Guyot F., Gautron L., Combes R., Hammouda T., Borenstajn S., Frost D. J., and Martinez I. (2004) Si in the core? New high pressures and high temperature experimental data. *Geochim. Cosmochim. Acta* **68**, 4201–4211.

Maxwell J. A., Campbell W. J., and Teesdale J. X. (1989) The Guelph PIXE software package. *Nucl. Instrum. Meth. B* **43**, 218–230.

McDade P., Wood B. J., Van Westrenen W., Brooker R., Gudmundsson G., Soulard H., Najorka J., and Blundy J. (2002) Pressure correction for a selection of piston-cylinder cell assemblies. *Mineral. Mag.* **66**(6), 1021–1028.

McDonough W. F. (2003) Compositional model for the Earth's core. In *Treatise on Geochemistry*, The Mantle and the Core, vol. 2 (ed. R. W. Carlson). pp. 547–568.

Moffatt W. G. (1984) In *The Handbook of Binary Phase Diagrams*, vol. 5, Genium Publishing Corporation.

Monchoux J. P., and Rabkin E. (2002) Microstructure evolution and interfacial properties in the Fe–Pb system. *Acta Mater.* **50**, 3159–3174.

Murthy V. R., van Westrenen W., and Fei Y. (2003) Experimental evidence that potassium is a substantial radioactive heat source in planetary cores. *Nature* **423**, 163–165.

Murrell M. T., and Burnett D. S. (1982) Actinide microdistributions in the enstatite meteorites. *Geochim. Cosmochim. Acta* **46**, 2453–2460.

Murrell M. T., and Burnett D. S. (1986) Partitioning of K, U, and Th between sulfide and silicate liquids: implications for radioactive heating of planetary cores. *J. Geophys. Res.* **91**, 8126–8136.

Musselwhite D. S., Dalton H. A., Keifer W. H., and Treiman A. H. (2006) Experimental petrology of the basaltic Shergottite Yamato 980459: implications for the thermal structure of the Martian Mantle. *Meteorit. Planet. Sci.* **41**, 1271–1290.

Mysen B. O., and Virgo D. (1980) Trace element partitioning and melt structure: an experimental study at 1 atm pressure. *Geochim. Cosmochim. Acta* **44**, 1917–1930.

Nimmo F., and Stevenson D. J. (2000) Influence of early plate tectonics on the thermal evolution and magnetic field of Mars. *J. Geophys. Res.* **105**, 11969–11979.

Nishihara Y., Aoki I., Takahashi E., Matsukage K. N., and Funakoshi K. (2005) Thermal equation of state of majorite with MORB composition. *Phys. Earth Planet. Int.* **147**, 73–84.

Ohtani E., and Yurimoto H. (1996) Element partitioning between metallic liquid, magnesiowüstite and silicate liquid at 20 GPa and 2500 °C: a secondary ion mass spectrometric study. *Geophys. Res. Lett.* **23**, 1993–1996.

Ohtani E., Yurimoto H., and Seto S. (1997) Element partitioning between metallic liquid, silicate liquid, and lower-mantle minerals: implications for core formation of the Earth. *Phys. Earth Planet. Int.* **100**, 97–114.

Okamoto, H. (1990) C–Fe (Carbon–Iron), second ed. In *Binary Alloy Phase Diagrams* (ed. T. B. Massalski). ASM International, pp. 842–848.

O'Neill H. St. C., Canil D., and Rubie D. (1998) Oxide-metal equilibra to 2500 °C and 25 GPa: Implications for core formation and the light component in the Earth's core. *J. Geophys. Res.* **103**(B6), 12239–12260.

Palme H., and O'Neill H. St. C. (2003) Cosmochemical estimates of mantle composition, In *Treatise on Geochemistry*, The Mantle and the Core, vol. 2 (ed. R.W. Carlson). pp. 1–38.

Perez W. A., and Dunn T. (1996) Diffusivity of strontium, neodymium and lead in natural rhyolite at 1.0 GPa. *Geochim. Cosmochim. Acta* **60**, 1387–21397.

Poirier J. P. (1994) Light elements in the Earth's outer core : a critical review. *Phys Earth Planet. Int.* **85**, 319–337.

Raghavan V. (1988) *Phase Diagrams of Ternary Iron Alloys. Part 2: Ternary Systems Containing Iron and Sulphur*. The Indian Institute of Metals, Calcutta.

Righter K., and Drake M. J. (1997) Metal/silicate equilibrium in a homogeneously accreting Earth: new results for Re. *Earth Planet. Sci. Lett.* **146**, 541–553.

Righter K., and Drake M. J. (2000) Metal/silicate equilibrium in the early Earth: new constraints from volatile moderately siderophile elements Ga, Sn, Cu and P. *Geochim. Cosmochim. Acta* **64**, 3581–3597.

Righter K. (2003) Metal/silicate partitioning of siderophile elements and core formation in the early Earth. *Ann. Rev. Earth Planet. Sci.* **31**, 135–174.

Rubie D. C., Melosh H. J., Reid J. E., and Liebske C. (2002) Mechanisms of metal/silicate equilibrium in the terrestrial magma ocean. *Earth Planet. Sci. Lett.* **205**, 239–255.

Rubie D. C., Gessmann C. K., and Frost D. J. (2004) Partitioning of oxygen during core formation on the Earth and Mars. *Nature* **429**, 58–61.

Sanloup C., and Fei Y. (2004) Closure of the Fe–S–Si liquid miscibility gap at high pressure. *Phys. Earth Planet. Int.* **147**, 57–65.

Schlesinger M. E., and Xiang Q. (2001) Enthalpies of mixing in Fe–C–Si melts. *J. Alloys Compd.* **321**, 242–247.

Seitz M. G. (1973) Uranium and thorium diffusion in diopside and fluorapatite. *Carnegie Inst. Washington Year Book* **72**, 586–588.

Sharma R. C., and Chang Y. A. (1979) Thermodynamics and phase relationships of transition metal–sulfur systems: Part III: thermodynamic properties of the Fe–S liquid phase and the calculation of the Fe–S phase diagram. *Met. Trans.* **10B**, 103–108.

Siebert J., Malavergne V., Guyot F., Combes R., and Martinez I. (2004) The behaviour of sulphur in metal–silicate core segregation experiments under reducing conditions. *Phys. Earth Planet. Int.*, 421–432.

Stevenson D. J. (1990) Fluid dynamics of core formation. In *Origin of the Earth* (eds. H. E. Newson and J. H. Jones). Oxford University Press, New York, pp. 231–249.

Tronnes R. G., and Frost D. J. (2002) Peridotite melting and mineral-melt partitioning of major and minor elements at 22–245 GPa. *Earth Planet. Sci. Lett.* **197**, 117–131.

Tsuno K., Ohtani E., and Terasaki H. (2007) Immiscible two-liquid regions in the Fe–O–S system at high pressure: Implications for planetary cores. *Phys. Earth Planet. Int.* **160**, 75–85.

Usselman T. M. (1975) Experimental approach to the state of the core: Part I. The liquidus relations of the Fe-rich portion of the Fe–Ni–S system from 30 to 100 kb. *Am. J. Sci.* **275**, 278–290.

Van Orman J. A., Grove T. L., and Shimizu N. (1998) Uranium and thorium diffusion in diopside. *Earth Planet. Sci. Lett.* **160**, 505–519.

Van Westrenen W., Blundy J., and Wood B. (1999) Crystal-chemical controls on trace element partitioning between garnet and anhydrous silicate melt. *Am. Mineral.* **84**, 838–847.

Wade J., and Wood B. J. (2005) Core formation and the oxidation state of the Earth. *Earth Planet. Sci. Lett.* **236**, 78–95.

Waldner P., and Pelton A. D. (2005) Thermodynamic modeling of the Fe–S system. *J. Phase Equilib. Diffus.* **26**, 23–38.

Walker D., and Agee C. B. (1989) Partitioning "equilibrium", temperature gradients, and constraints on Earth differentiation. *Earth. Planet. Sci. Lett.* **96**, 49–60.

Wänke H., Dreibus G., and Jagoutz E. (1984) Mantle chemistry and accretion history of the Earth. *Archean Geochemistry*, pp. 1–24. Springer, Berlin.

Wänke H., and Dreibus G. (1994) Chemistry and accretion history of Mars. *Phil. Trans. R. Soc. London* **A349**, 285–293.

Wasserburg G. J., MacDonald G. J. F., Hoyle F., and Fowler W. A. (1964) Relative contributions of uranium, thorium and potassium to heat production in the Earth. *Science* **143**, 465–467.

Wheeler K. T., Walker D., Fei Y., Minarik W., and McDonough W. (2006) Experimental partitioning of Uranium between liquid iron sulfide and liquid silicate: implications for radioactivity in the Earth's core. *Geochim. Cosmochim. Acta* **70**, 1537–1547.

Williams J. P., and Nimmo F. (2004) Thermal evolution of the Martian core: implication for an early dynamo. *Geology* **32**, 97–100.

Wood B. J., and Halliday A. N. (2005) Cooling of the Earth and core formation after the giant impact. *Nature* **437**, 1345–1348.

Yukutake T. (2000) The inner core and the surface heat flow as clues to estimating the initial temperature of the Earth's core. *Phys. Earth Planet. Interiors* **121**, 103–137.

Zhang J., and Herzberg C. (1994) Melting experiments on anhydrous peridotite KLB-1 from 5.0 to 22.5 GPa. *J. Geophys. Res.* **99**, 17729–17742.

Zheng H., Ma W., Zheng C., Guo X., and Li J. (2003) Rapid solidification of undercooled monotectic alloy melts. *Mater. Sci. Eng.* **A355**, 7–13.

Zheng H., Yun Y., and Jianguo L. (2005) Microstructural evolution of undercooled Ni–40 wt%Pb hypermonotectic alloy. *Mater. Sci. Forums*, 2651–2654.

Associate editor: Brent Poe